

The Shape of Dark Matter Halos: Dependence on Mass, Redshift, Radius, and Formation

Brandon Allgood¹, Ricardo A. Flores², Joel R. Primack¹, Andrey V. Kravtsov³, Risa H. Wechsler^{3,4}, Andreas Faltenbacher⁵, and James S. Bullock⁶

¹*Physics Department, University of California, Santa Cruz, CA 95064; allgood@physics.ucsc.edu, joel@scipp.ucsc.edu*

²*Department of Physics and Astronomy, University of Missouri – St. Louis, St. Louis, MO 63121; ricardo.flores@umsl.edu*

³*Dept. of Astronomy and Astrophysics, Kavli Institute for Cosmological Physics, and The Enrico Fermi Institute,*

The University of Chicago, Chicago, IL 60637; andrey@oddjob.uchicago.edu, risa@cfcp.uchicago.edu

⁴*Hubble Fellow, Enrico Fermi Fellow*

⁵*Lick Observatory, University of California, Santa Cruz, CA 95064; fal@ucolick.org*

⁶*Center for Cosmology, Department of Physics and Astronomy, University of California, Irvine, CA 92697; bullock@uci.edu*

14 September 2018

ABSTRACT

Using six high resolution dissipationless simulations with a varying box size in a flat LCDM universe, we study the mass and redshift dependence of dark matter halo shapes for $M_{\text{vir}} = 9.0 \times 10^{11} - 2.0 \times 10^{14}$, over the redshift range $z = 0 - 3$, and for two values of $\sigma_8 = 0.75$ and 0.9 . Remarkably, we find that the redshift, mass, and σ_8 dependence of the mean smallest-to-largest axis ratio of halos is well described by the simple power-law relation $\langle s \rangle = (0.54 \pm 0.02)(M_{\text{vir}}/M_*)^{-0.050 \pm 0.003}$, where s is measured at $0.3R_{\text{vir}}$ and the z and σ_8 dependences are governed by the characteristic nonlinear mass, $M_* = M_*(z, \sigma_8)$. We find that the scatter about the mean s is well described by a Gaussian with $\sigma \sim 0.1$, for all masses and redshifts. We compare our results to a variety of previous works on halo shapes and find that reported differences between studies are primarily explained by differences in their methodologies. We address the evolutionary aspects of individual halo shapes by following the shapes of the halos through ~ 100 snapshots in time. We determine the formation scalefactor a_c as defined by Wechsler et al. (2002) and find that it can be related to the halo shape at $z = 0$ and its evolution over time.

Key words: cosmology: theory — galaxies: formation — galaxies: halos — large-scale structure of universe

1 INTRODUCTION

A generic prediction of cold dark matter (CDM) theory is the process of bottom up halo formation, where large halos form from the mergers of smaller halos, which are in turn formed from even smaller halos. This is a violent process and it violates most of the assumptions that go into the spherical top-hat collapse model of halo formation which is often used to describe halos. Since mass accretion onto halos is often directional and tends to be clumpy, one would not expect halos to be spherical if the relaxation time of the halos were longer than the time between mergers and/or if the in-falling halos came along a preferential direction (such as along a filament). In both theoretical modelling of CDM and observations, halos are found to be very non-spherical. In fact, spherical halos are rare. Therefore, the analysis of

halo shapes can give us another clue to the nature of the dark matter and the process of halo and galaxy formation.

One way of quantifying the shape of a halo is to go one step beyond the spherical approximation and approximate halos by ellipsoids. Ellipsoids are characterised by three axes, a, b, c , with $a \geq b \geq c$, which are normally described in terms of ratios, $s \equiv c/a$, $q \equiv b/a$, and $p \equiv c/b$. Ellipsoids can also be described in terms of three classes, which have corresponding ratio ranges: prolate (sausage shaped) ellipsoids have $a > b \approx c$ leading to axial ratios of $s \approx q < p$, oblate (pancake shaped) ellipsoids have $a \approx b > c$ leading to axial ratios of $s \approx p < q$, and triaxial ellipsoids are in between prolate and oblate with $a > b > c$. Additionally, when talking about purely oblate ellipsoids, $a = b$, it is common to use just q , since s and q are degenerate.

There have been many theoretical papers published over the years which examined the subject

of halo shapes. The early work on the subject includes Barnes & Efstathiou (1987); Dubinski & Carlberg (1991); Katz (1991); Warren et al. (1992); Dubinski (1994); Jing et al. (1995); Tormen (1997); Thomas et al. (1998). All of these works agreed that halos are ellipsoidal, but otherwise differ in several details. Dubinski & Carlberg (1991) found that halos have axial ratios of $s \sim 0.5$ in the interior and become more spherical at larger radii, while Frenk et al. (1988) found that halos are slightly more spherical in the centres. Thomas et al. (1998) claimed that larger mass halos have a slight tendency to be more spherical, where more recent simulation results find the opposite. Despite these disagreements many of the early authors give us clues into the nature of halo shapes. Warren et al. (1992) and Tormen (1997) showed that the angular momentum axis of a halo is well correlated with the smallest axis, c , although, as most of these authors pointed out, halos are not rotationally supported. This therefore has led many to conclude that the shapes are supported by anisotropic velocity dispersion. Tormen (1997) took it one step further and found that the velocity anisotropy was in turn correlated with the infall anisotropy of merging satellites. Most authors found that the axial ratios of halos are $\sim 0.5 \pm 0.1$ and that halos tend to be prolate as opposed to oblate in shape. The most likely source of the disagreement in these works and in the more recent works we describe below is the different methods used often coupled with inadequate resolution.

More recent studies of halos' shape were performed by Bullock (2002); Jing & Suto (2002); Springel, White & Hernquist (2004); Bailin & Steinmetz (2005); Kasun & Evrard (2004); Hopkins et al. (2005). The results of these authors differ, in some cases, considerably. One of the goals of this paper is to carefully examine the differences in the findings presented by the above authors.

All of the aforementioned publications (except Springel et al. 2004) analyse simulations with either no baryons or with adiabatic hydrodynamics. This is both due to the cost associated with performing self consistent hydrodynamical simulations of large volumes with high mass resolution and due to the fact that very few cosmological simulations yet produce realistic galaxies. Nonetheless, we know that the presence of baryons should have an effect on the shapes of halos due to their collisional behaviour. Three recent papers have attempted to examine the effect of baryons (Springel et al. 2004; Kazantzidis et al. 2004; Bailin et al. 2005). In Springel et al. (2004) the same simulations were done using no baryons, adiabatic baryons and baryons with cooling and star formation. In the first two cases there was very little difference, but with the presence of cooling and star formation the halos became more spherical. The radial dependence of shape also changes such that the halo is more spherical in the centre. At $R > 0.3R_{\text{vir}}$ the axial ratio s increases by ≤ 0.09 , but in the interior the increase Δs is as much as 0.2. In an independent study, Kazantzidis et al. (2004) found an even larger effect due to baryonic cooling in a set of 11 high resolution clusters. At $R = 0.3R_{\text{vir}}$ the authors found that s can increase by 0.2 – 0.3 in the presence of gas cooling. The extent of the over-cooling problem plaguing these simulations is still uncertain. This amount of change in the shape should be viewed as an upper limit. The most recent work on the subject is Bailin et al. (2005), who concentrate more on the

relative orientation of the galaxy formed at the centre of eight high resolution halos than on the relative sphericity of the halos. Despite this, from Figure 1 of Bailin et al. (2005) it seems that they would also predict an increase of ~ 0.2 for s . It is still useful to study shapes of halos without baryonic cooling. Cooling and star formation in simulations is still a very open question, making the effect of the cooling uncertain. We show in Paper II that our simulations without cooling match shapes of X-ray clusters.

Measurements of the shapes of both cluster and galaxy mass halos through varied observational techniques are increasingly becoming available. There have been many studies of the X-ray morphologies of clusters (see McMillan, Kowalski & Ulmer 1989; Mohr, Evrard, Fabricant & Geller 1995; Kolokotronis, Basilakos, Plionis & Georgantopoulos 2001) which can be directly related to the shape of the inner part of the cluster halo (Lee & Suto 2003; Buote & Xu 1997). For a review of X-ray cluster shapes and the latest results, see Flores et al. (2005), hereafter referred to as Paper II.

There has also been important new information on the shape of galaxy mass halos, in particular our own Milky Way halo. Olling & Merrifield (2000) concluded that the host halo around the Galactic disk is oblate with a short-to-long axial ratio of $0.7 < q < 0.9$. Investigations of Sagittarius' tidal streams have led to the conclusion that the Milky Way halo is oblate and nearly spherical with $q \gtrsim 0.8$ (Ibata et al. 2001; Majewski et al. 2003; Martínez-Delgado et al. 2004). However, by inspecting M giants within the leading stream Helmi (2004) and Law, Johnston & Majewski (2005) found a best fit prolate halo with $s = 0.6$. Merrifield (2004) summarises the currently reliable observations for galaxy host halo shapes using multiple techniques and find that the observations vary a lot.

Another method for studying shapes of halos at higher redshift is galaxy-galaxy weak lensing studies. Analysing data taken with the Canada-France-Hawaii telescope, Hoekstra, Yee & Gladders (2004) find a signal at a 99.5% confidence level for halo asphericity. They detect an average projected ellipticity of $\langle \epsilon \rangle \equiv (1 - q_{2D}) = 0.20^{+0.04}_{-0.05}$, corresponding to $s = 0.66^{+0.07}_{-0.06}$, for halos with an average mass of $8 \times 10^{11} h^{-1} M_{\odot}$. Ongoing studies of galaxy-galaxy weak lensing promise rapidly improving statistics from large scale surveys like the Canada-France Legacy survey.

This paper is organised as follows: In Section 2 we describe the simulations, halo finding method, and halo property determination methods used in this study. In Section 3 we discuss the method used to determine the shapes of halos. In Section 4 we examine the mean axial ratios from our simulations and their dependence on mass, redshift and σ_8 . We then examine the dispersion of the axial ratio versus mass relation. We briefly discuss the shape of halos as a function of radius and then examine the relationship of the angular momentum and velocity anisotropy to the halo shape. In Section 5 we examine the relationship between the formation history of halos and their present day shapes. In Section 6 we compare our results to those of previous authors and explain the sources of the differences. In section 7 we examine the observational tests and implications of our findings. Finally, Section 8 is devoted to summary and conclusions.

Table 1. Simulation parameters

Name	σ_8	Ω_b	L_{box} $h^{-1}\text{Mpc}$	N_p	m_p $h^{-1} M_\odot$	h_{peak} $h^{-1} \text{kpc}$	$z = 0$	$M_*(10^{12}h^{-1} M_\odot)$			
								$z = 1$	$z = 2$	$z = 3$	
L80 _{0.75}	0.75	0.030	80	512 ³	3.16×10^8	1.2	3.0	0.11	0.0046	0.00027	
L80 _{0.9a}	0.9	0.045	80	512 ³	3.16×10^8	1.2	8.0	0.35	0.019	0.0013	
L80 _{0.9b}	0.9	0.045	80	512 ³	3.16×10^8	1.2	8.0	0.35	0.019	0.0013	
L200 _{0.9}	0.9	0.030	200	256 ³	3.98×10^{10}	5.0	8.6	0.41	0.023	0.0018	
L120 _{0.9}	0.9	0.045	120	512 ³	1.07×10^9	1.8	8.0	0.35	0.019	0.0013	
L120 _{0.9r}	0.9	0.045	40 sphere	$\sim 256^3$	1.33×10^8	0.9	8.0	0.35	0.019	0.0013	

2 SIMULATIONS

2.1 The Numerical Simulations

All our simulations (see Table 1) were performed with the Adaptive Refinement Tree (ART) N-body code of Kravtsov, Klypin & Khokhlov (1997) which implements successive refinements in both the spacial grid and time step in high density environments. We analyse the shapes of halos and their merger histories in the concordance flat Λ CDM cosmological model: $\Omega_m = 0.3 = 1 - \Omega_\Lambda$, $h = 0.7$, where Ω_m and Ω_Λ are the present-day matter and vacuum energy densities in units of critical density and h is the Hubble parameter in units of $100\text{km s}^{-1}\text{Mpc}^{-1}$. The power spectra used to generate the initial conditions for the simulations were determined from a direct Boltzmann code calculation (courtesy of Wayne Hu).

To study the effects of the power spectrum normalisation and resolution, we consider five simulations of the Λ CDM cosmology. The first simulation (L80_{0.75}) followed the evolution of $512^3 = 1.34 \times 10^8$ particles in a $80h^{-1}\text{Mpc} = 114.29\text{Mpc}$ box and was normalised to $\sigma_8 = 0.75$, where σ_8 is the rms fluctuation in spheres of $8h^{-1}\text{Mpc}$ comoving radius. The second simulation (L80_{0.9}) is an exact replica of the L80_{0.75} simulation with the same random number seed, but the power spectrum was normalised to $\sigma_8 = 0.9$. The first simulation was also used to study the halo occupation distribution and the physics of galaxy clustering by Kravtsov et al. (2004) and Zentner et al. (2005a). Unfortunately, both of these simulations were generated with a power spectrum which had a little more than average power on large scales. This may happen when generating power spectra due to cosmic variance. The simulation is still a good representation of a volume in the Universe, but to avoid becoming non-linear on large scales, the second simulation was stopped at $z = 0.1$. Due to the lower normalisation of the L80_{0.75} box it was allowed to run until $z = 0$. We use these two simulations to study the effects of the spectrum normalisation, but to achieve better statistics and make predictions for $\sigma_8 = 0.9$ at $z = 0$ we also include another simulation of the same size and resolution (L80_{0.9b}). The fourth simulation (L200_{0.9}) followed the evolution of $256^3 = 1.68 \times 10^7$ particles in a $200h^{-1}\text{Mpc} = 285.7\text{Mpc}$ box. The fifth simulation L120_{0.9} followed the evolution of 512^3 particles in a $120h^{-1}\text{Mpc} = 171.43\text{Mpc}$ box and was normalised to

$\sigma_8 = 0.9$. This simulation is used for several purposes: firstly to achieve better statistics for rare high mass objects, and secondly as the basis for the sixth simulation. The sixth simulation is a resimulated Lagrangian subregion of the L120_{0.9} box corresponding at $z = 0$ to a sphere in position space of diameter $D = 40h^{-1}\text{Mpc}$. The initial conditions of the L120_{0.9} box initially contained 1024^3 particles which were combined into 512^3 particles used for the initial simulation. The Lagrangian subregion was then chosen and the original higher resolution particles of mass $m_p = 1.33 \times 10^8 h^{-1} M_\odot$ within this region, corresponding to 1024^3 particles in the box, were followed from the initial time step, $z_i = 40$. The high mass resolution region was surrounded by layers of particles of increasing mass with a total of five particle species in order to preserve the large scale gravitational field. Only the regions containing the highest resolution particles were adaptively refined. The maximum level of refinement in the simulation corresponded to a peak formal spatial resolution of $0.9h^{-1}\text{kpc}$. For more details about the multi-mass technique consult Klypin et al. (2001). The subregion was chosen not to contain any halos above $M_{\text{vir}} > 10^{13}h^{-1} M_\odot$ in order to increase the statistics of isolated galaxy mass halos.

2.2 Halo Identification and Classification

A variant of the Bound Density Maximum (BDM) algorithm is used to identify halos and subhalos in our simulations (Klypin et al. 1999). The details of the algorithm and parameters being used in the halo finder can be found in Kravtsov et al. (2004). We briefly describe the main steps in the halo finder here. First, all particles are assigned a density using the smooth algorithm¹, which uses a symmetric SPH (Smoothed Particle Hydrodynamics) smoothing kernel on the 32 nearest neighbours. Density maxima are then identified which are separated by a minimum distance of $r_{\text{min}} = 50h^{-1}\text{kpc}$, defining the minimum distinguishable separation of halos and subhalos. Using the maxima as centres, profiles in circular velocity and density are calculated in spherical bins. Unbound particles are removed iteratively as described in Klypin et al. (1999). The halo catalogue used is

¹ To calculate the density we use the publicly available code `smooth`: <http://www-hpcc.astro.washington.edu/tools/tools.html>

complete for halos with $\gtrsim 50$ particles. This corresponds to a mass below which the cumulative mass and velocity functions begin to flatten (see Kravtsov et al. (2004) for details).

The halo density profiles are constructed using only bound particles and they are fit by an NFW profile (Navarro et al. 1996):

$$\rho_{\text{NFW}}(r) = \frac{\rho_s}{(r/r_s)(1+r/r_s)^2}, \quad (1)$$

where r_s is the radius at which the log density profile has a slope of -2 and the density is $\rho_s/4$. One of the parameters, r_s or ρ_s , can be replaced by a virial parameter ($R_{\text{vir}}, M_{\text{vir}}$, or V_{vir}) defined such that the mean density inside the virial radius is Δ_{vir} times the mean universal density $\rho_o(z) = \Omega_m(z)\rho_c(z)$ at that redshift:

$$M_{\text{vir}} = \frac{4\pi}{3}\Delta_{\text{vir}}\rho_o R_{\text{vir}}^3 \quad (2)$$

where $\rho_c(z)$ is the critical density, and

$$\Delta_{\text{vir}}(z) = \frac{18\pi^2 + 82(\Omega_m(z) - 1) - 39(\Omega_m(z) - 1)^2}{\Omega_m(z)} \quad (3)$$

from Bryan & Norman (1998) with $\Delta_{\text{vir}}(0) \approx 337$ for the Λ CDM cosmology assumed here. The NFW density profile fitting is performed using a χ^2 minimisation algorithm. The profiles are binned logarithmically from twice the resolution length (see Table 1) out to R_{500} , the radius within which the average density is equal to 500 times the critical density of the universe. The choice of this outer radius is motivated by Tasitsiomi et al. (2004) who showed that halos are well relaxed within this radius. The binning begins with 10 radial bins. The number of bins is then reduced if any bin contains fewer than 10 particles or is radially smaller than the resolution length. This reduction of bins is continued until both criteria are met. Fits using this method have been compared to fits determined using different merit functions, such as the maximum deviation from the fit as described in Tasitsiomi et al. (2004) and it was found that they give very similar results for individual halos. After fitting the halos the host halo and subhalo relationship is determined very simply. If a halo's centre is contained within the virial radius of a more massive halo, that halo is considered a subhalo of the larger halo. All halo properties reported here are for halos which are determined to be isolated or host halos (i.e., not subhalos).

3 METHODS OF DETERMINING SHAPES

There are many different methods to determine shapes of halos. All methods model halos as ellipsoidal with the eigenvectors of some form of the inertia tensor corresponding to the axes $c \leq b \leq a$ ($s \equiv c/a$ and $q \equiv b/a$). The two forms of the inertia tensor used in the literature to determine shape are the unweighted,

$$I_{ij} \equiv \sum_n x_{i,n}x_{j,n} \quad (4)$$

and the weighted (or reduced),

$$\tilde{I}_{ij} \equiv \sum_n \frac{x_{i,n}x_{j,n}}{r_n^2} \quad (5)$$

where

$$r_n = \sqrt{x_n^2 + y_n^2/q^2 + z_n^2/s^2}, \quad (6)$$

is the elliptical distance in the eigenvector coordinate system from the centre to the n th particle. In both cases the eigenvalues ($\lambda_a \leq \lambda_b \leq \lambda_c$) determine the axial ratios described at the beginning of Section 1 with $(a, b, c) = \sqrt{\lambda_a, \lambda_b, \lambda_c}$. The orientation of the halo is determined by the corresponding eigenvectors.

One would like to recover the shape of an isodensity surface. The method used here begins by determining \tilde{I} with $s = 1$ and $q = 1$, including all particles within some radius. Subsequently, new values for s and q are determined and the volume of analysis is deformed along the eigenvectors in proportion to the eigenvalues. There are two options to choose from when deforming the volume. The volume within the ellipsoid can be kept constant, or one of the eigenvectors can be kept equal to the original radius of the spherical volume. In our analysis of shapes, the longest axis is kept equal to the original spherical radius. After the deformation of the original spherical region, \tilde{I} is calculated once again, but now using the newly determined s and q and only including the particles found in the new ellipsoidal region. The iterative process is repeated until convergence is achieved. Convergence is achieved when the variance in both axial ratios, s and q , is less than a given tolerance.

The analysis presented here begins with a sphere of $R = 0.3R_{\text{vir}}$, and keeps the largest axis fixed at this radius unless otherwise stated. For determining halo shapes accurately we limit our analysis to isolated halos with $N_p \geq 7000$ within R_{vir} . This corresponds to $M_{\text{vir}} \geq 2.21 \times 10^{12} h^{-1} M_\odot$ for the $80h^{-1}\text{Mpc}$ box simulations, $M_{\text{vir}} \geq 7.49 \times 10^{12} h^{-1} M_\odot$ for the $120h^{-1}\text{Mpc}$ box simulation, and $M_{\text{vir}} \geq 9.3 \times 10^{11} h^{-1} M_\odot$ in the resimulated region of the $120h^{-1}\text{Mpc}$ box. For a discussion of our resolution tests, see Appendix A.

4 SHAPES AS A FUNCTION OF HALO MASS

The simulations analysed here enable us to analyse halos spanning a mass range from galaxy to cluster sized objects. These data provide an opportunity to study the variation of shape and its intrinsic scatter with halo mass. Various statistics are used to derive robust estimates of the dependence of shape on halo-centric radius. Combining the detailed spatial and dynamical information from the simulations we can relate quantities like angular momentum or velocity anisotropy tensor to the shape and the orientation of the halo. In this section we aim to present a comprehensive analysis of the properties of halos at all redshifts. In section 5 we will address evolutionary aspects of individual halo shapes.

4.1 Median Relationships for Distinct Halos

We begin by fitting the mass dependence of halo shape and find that the mean value of the axial ratio $s \equiv c/a$ decreases monotonically with increasing halo mass as illustrated in Figure 1. In other words, less massive halos have a more spherical mean shape than more massive halos. Since we use four different simulations (L80_{0.96}, L120_{0.9}, L120_{0.9r}, and

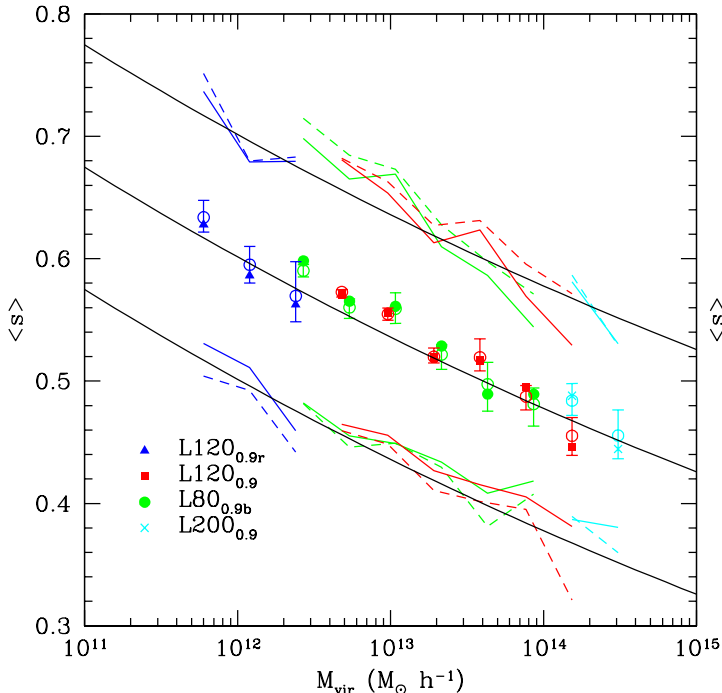


Figure 1. Mean axial ratios $s = c/a$ for four simulations of different mass resolution are presented with a fit (solid black lines) given by Equation (7) and dispersion of 0.1. The triangles, squares, solid circles and \times symbols are the average s for a given mass bin. The solid circles have been shifted by 0.05 in log for clarity. The open circles and error bars are the best fit Kolmogorov-Smirnov mean and 68% confidence level assuming a Gaussian parent distribution. The dashed lines connect the raw dispersion for each point and the coloured solid lines are the best fit (KS test) dispersion. (See the electronic edition for colour version of the figure)

L200_{0.9}) with varying mass and length scales we are able to determine $\langle s \rangle(M_{\text{vir}})$ over a wide mass range. We find that over the accessible mass range the variation of shape with halo mass is well described by

$$\langle s \rangle(M_{\text{vir}}, z = 0) = \alpha \left(\frac{M_{\text{vir}}}{M_*} \right)^\beta \quad (7)$$

with best fit values

$$\alpha = 0.54 \pm 0.03, \quad \beta = -0.050 \pm 0.003. \quad (8)$$

The parameters, α and β were determined by weighted χ^2 minimisation on the best fit mean data points determined via Kolmogorov-Smirnov (KS) analysis assuming a Gaussian distribution within a given mass bin (see section 4.4). $M_*(z)$ is the characteristic nonlinear mass at z such that the rms top-hat smoothed overdensity at scale $\sigma(M_*, z)$ is $\delta_c = 1.68$. The M_* for $z = 0$ is $8.0 \times 10^{12} h^{-1} M_{\odot}$ for the simulations with $\Omega_b = 0.045$ and 8.6×10^{12} for the simulations with $\Omega_b = 0.03$. Only bins containing halos above our previously stated lower bound resolution limit were used and only mass bins with at least 20 halos were included in the fit. This work extends the mass range of the similar relationships found by previous authors (Jing & Suto 2002; Bullock 2002; Springel et al. 2004; Kasun & Evrard 2004); we compare our results with these previous works in Section 6.

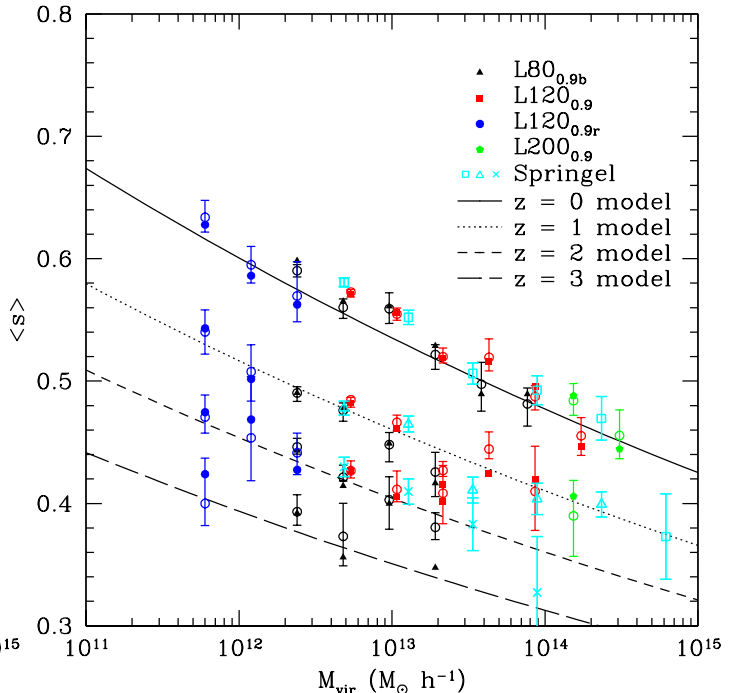


Figure 2. $\langle s \rangle(M)$ for $z = 0.0, 1.0, 2.0, 3.0$. The binning is the same as in Figure 1, but now for many different redshifts. The solid line is the power-law relation set out in Equation (7). The L120_{0.9} points are shifted by 0.05 in log for clarity. The Springel data agrees quite well with our data and model for $z = 0.0, 1.0, 2.0$.

4.2 Shapes of Halos at Higher Redshifts

The use of M_* in the Equation (7) alludes to the evolution of the $\langle s \rangle(M_{\text{vir}})$ relation. After examining the $\langle s \rangle(M_{\text{vir}})$ relation at higher redshifts, we find that the relation between $\langle s \rangle$ and M_{vir} is successfully described by Equation (7) with the appropriate $M_*(z)$. The M_* for $z = 1.0, 2.0$, and 3.0 are $3.5 \times 10^{11}, 1.8 \times 10^{10}$, and $1.3 \times 10^9 h^{-1} M_{\odot}$ respectively for the simulations with $\Omega_b = 0.045$. We present our results for various redshifts in Figure 2 from the L120_{0.9r}, L80_{0.9}, L120_{0.9} and L200_{0.9} simulations. We have also included data points provided to us by Springel (private communication) in Figure 2 for comparison, which from a more complete sample than the data presented in Springel et al. (2004) and are for shapes measured at $0.4R_{\text{vir}}$.

4.3 Dependence on σ_8

Of the parameters in the Λ CDM cosmological model the parameter which is the least constrained and the most uncertain is the normalisation of the fluctuation spectrum, usually specified by σ_8 . Therefore, it is of interest to understand the dependence of the $\langle s \rangle(M_{\text{vir}})$ relation on σ_8 . Since M_* is dependent on σ_8 the scaling with M_* in Equation (7) may already be sufficient to account for the σ_8 dependence. As stated in Section 2, L80_{0.75} and L80_{0.9a} were produced with the same Gaussian random field but different values for the normalisation. Therefore the differences between the two simulations can only be a result of the different values

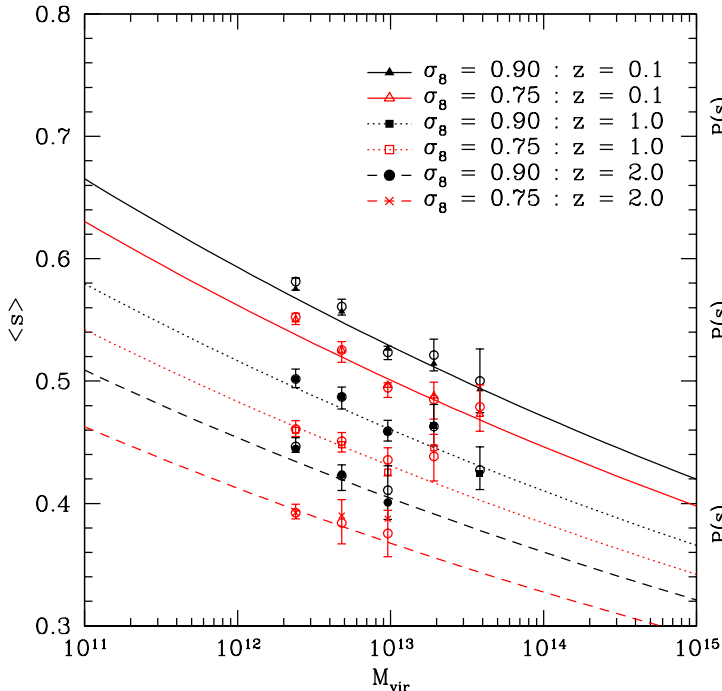


Figure 3. $\langle s \rangle$ vs M with different values of σ_8 . Different values of σ_8 predict different values for the $\langle s \rangle$ vs M relationship. Here one can see that a universe with a lower σ_8 produces halos which are more elongated, although the power-law relationship (Equation (7)) remains valid, as shown by the agreement between the points and the lines representing this prediction.

for σ_8 . As Figure 3 illustrates, the two simulations do indeed produce different relations. We find that the M_* dependence in Equation (7) is sufficient to describe the differences between simulations of different σ_8 . One should expect this from the result of the previous subsection, that the redshift evolution was also well described by the M_* dependence. The values of M_* for $z = 0.1$ are 5.99×10^{12} for $\sigma_8 = 0.9$ and 2.22×10^{12} for $\sigma_8 = 0.75$. The value of M_* for $\sigma_8 = 0.75$ at $z = 1$ and 2 are 1.09×10^{11} and 4.57×10^9 respectively. A simple fit to the redshift dependence of M_* in these cosmologies is $\log(M_*) = A - B \log(1+z) - C(\log(1+z))^2$, with $A(B, C) = 12.9(2.68, 5.96)$ for $\sigma_8 = 0.9$ and $A(B, C) = 12.5(2.94, 6.28)$ for $\sigma_8 = 0.75$, and accurate to within 1.6% and 3.1%, respectively, for $z \leq 3$.

4.4 Mean - Dispersion Relationship

In the previous subsections we used the best KS test fit mean, assuming a Gaussian parent distribution, as an estimate of the true mean of axial ratios within a given mass bin. In this subsection we examine the validity of this assumption, and test whether the dispersion has the mass dependence suggested by Jing & Suto (2002). In Figure 4 we present the distribution of s in the six bins from Figure 1 for L120_{0.9}. In each of the plots we have also included the KS best fit Gaussian, from which the mean was used to determine the best fit power-law in Equation (7). The error-bars on the mean indicated in Figure 1 are the 68% confidence limits of the KS probability. The limits are determined by

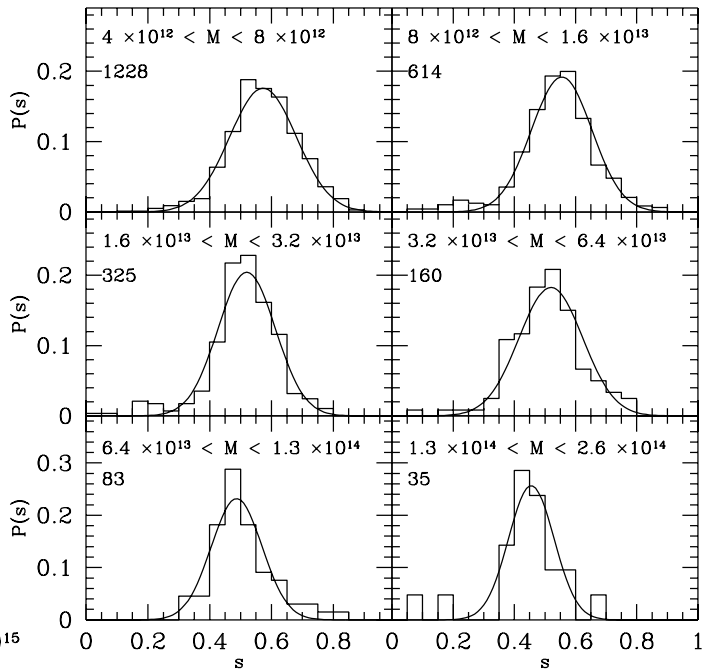


Figure 4. The distribution of s in the L120_{0.9b} simulation in the mass ranges indicated. The number of halos in each bin is also indicated. The Gaussian fit shown for each graph is the best fit, based on a KS test analysis.

varying the mean of the parent distribution until the KS probability drops below 16% for greater and less than the best fit value for the dispersion in each mass bin. The values from this analysis corresponding to the distributions in Figure 4 can be found in Table 2. In Figure 4 the lowest mass bin, which also contains the most halos, is well fit by a Gaussian. This is seen in Table 2 not only by the best fit KS probability, but also by the small range of the confidence limits. The higher mass bins are consistent with having Gaussian parent distributions though the parent distributions' values for the mean and dispersion are not as well constrained. There is no indication of a structured tail to lower values of s , but Table 3 indicates that the distributions have negative skewness. This arises from a small number of halos with very low values of s , which are always determined to be ongoing major mergers with very close cores.

Jing & Suto (2002) found that the distribution of s within a given mass bin is Gaussian. They found no indication of a tail or any low values of s . This is most likely due to their treatment of halos with multiple cores (see section 6). Bullock (2002) found a large tail to low values of s using $R = R_{\text{vir}}$. After repeating our analysis at $R = R_{\text{vir}}$ we find the exact opposite. We find even less indication of a tail than in the distributions shown in Figure 4. The difference is most likely due to the centres of halos determined by the different halo finders used. Bailin & Steinmetz (2005) find a more subtle but significant tail to lower values of s . This is most likely just a side effect of combining all mass bins into one histogram. If the histogram were divided into bins over smaller ranges in mass, this tail would be seen as a consequence of the combination of Gaussian distributions with

Table 2. Kolmogorov-Smirnov Best Fit Values

Mass ($h^{-1} M_{\odot}$)	$\langle s \rangle$	σ_s	KS Prob
4.8×10^{12}	0.583 (+0.003 -0.003)	0.108 (+0.006 -0.005)	0.80
9.6×10^{12}	0.554 (+0.006 -0.006)	0.110 (+0.005 -0.007)	0.61
1.92×10^{13}	0.518 (+0.009 -0.004)	0.094 (+0.007 -0.013)	0.72
3.84×10^{13}	0.519 (+0.014 -0.013)	0.108 (+0.016 -0.030)	0.95
7.68×10^{13}	0.486 (+0.005 -0.010)	0.082 (+0.020 -0.015)	0.78
1.54×10^{14}	0.467 (+0.012 -0.014)	0.073 (+0.050 -0.033)	0.93

the property that mass bins with a lower number of halos also have lower mean values, as in Figure 4. Kasun & Evrard (2004) find that the distribution about the mean “is well fit by a Gaussian” and contains no halos with low values of s . We find the same in our spherical window analysis.

Now we turn our attention to the relationship between $\langle s \rangle$ and the dispersion for each bin. At $z = 0$ we find a dependence of the dispersion on $\langle s \rangle$ (top plot in Figure 5). The relationship is steeper than that of Jing & Suto (2002), who determined that $\sigma_s = 0.21\langle s \rangle$ for the mass range they studied. However, one can see in the bottom plot of Figure 5 that at $z = 1$ this relationship is no longer visible. This may be due to the fact that the number of halos in each bin at $z = 1$ is much lower and therefore dominated by systematics. It could also be that a large enough range in mass is not probed at $z = 1$ to see the relationship. We are unable to draw a conclusion similar to Jing & Suto (2002). We therefore assume a constant value of $\sigma_s = 0.1$, which is consistent with our results at all redshifts.

4.5 Middle Axis Relationship

The largest to smallest axial ratio, s , does not uniquely determine an ellipsoidal shape. There is still the determination of the relationship of the middle axis (b) to the smallest (c) or largest (a) axis. We find in our analysis, as did Jing & Suto (2002), that the function $P(p \equiv c/b|s)$ exhibits a nice symmetric behaviour. More commonly examined is the distribution of $q \equiv b/a$ which can be trivially obtained from $P(p|s)$. Figure 6 contains six histograms of p for different ranges in s . The curves are a fit proposed by Jing & Suto (2002),

$$P(p|s) = \frac{3}{2(1-\tilde{s})} \left[1 - \left(\frac{2p-1-\tilde{s}}{1-\tilde{s}} \right)^2 \right] \quad (9)$$

with $\tilde{s} = s_{\min}$ for $s < s_{\min} = 0.55$ and $\tilde{s} = s$ for $s \geq s_{\min}$. It should also be noted that $P(p|s) = 0$ below \tilde{s} . Jing & Suto (2002) fit with a cut-off of $s_{\min} = 0.5$, but otherwise we find agreement with their results.

4.6 Radial Dependence of Shape

The ellipsoidal shape of a halo is also found to be dependent on the radius at which the shape is determined. There is a systematic dependence of shape on radius with more massive halos having a steeper gradient in s with radius than lower

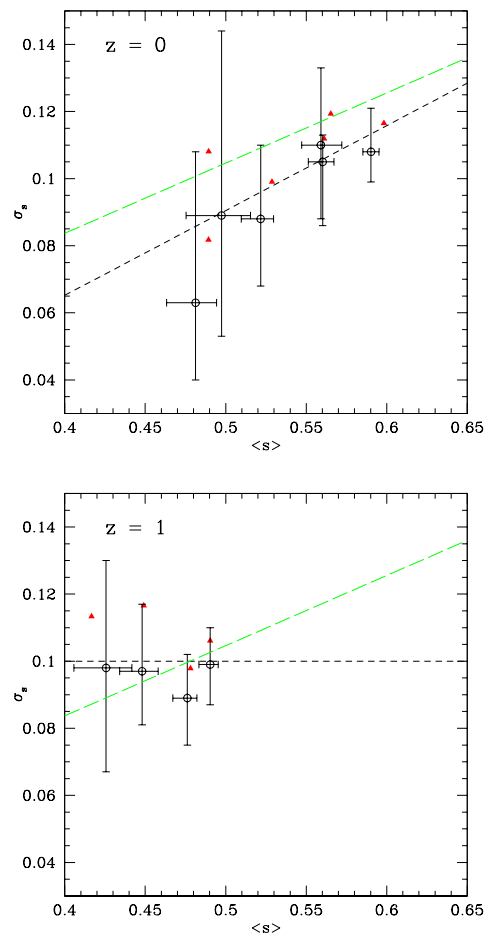


Figure 5. $\langle s \rangle$ versus σ_s . Top: We find some evidence for a dependence of the dispersion on $\langle s \rangle$ at $z = 0.0$ if we perform a weighted linear least squares fit to the best values (black circles) of $\langle s \rangle$ and $\sigma_{\langle s \rangle}$ (black short dashed line). It is slightly steeper than that of Jing & Suto (2002) (green long dashed line). Also shown are the raw average and dispersion points (red triangles) Bottom: By $z = 1.0$ this relationship seems to have disappeared. Due to the lack of a clear relationship between $\langle s \rangle$ and σ_s , we favour a constant value of $\sigma_s = 0.1$, which is consistent with all redshifts and is roughly consistent with Jing & Suto (2002) for the values of $\langle s \rangle$ probed.

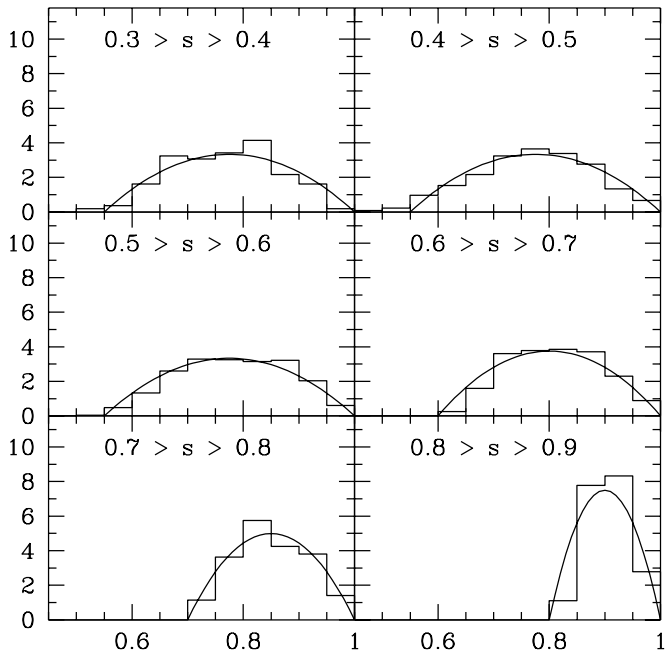


Figure 6. The distribution of $p = c/b$ in given bins of s shows a very similar behaviour to that found in Jing & Suto (2002). The fit line is from Equation (9), originally found in Jing & Suto (2002).

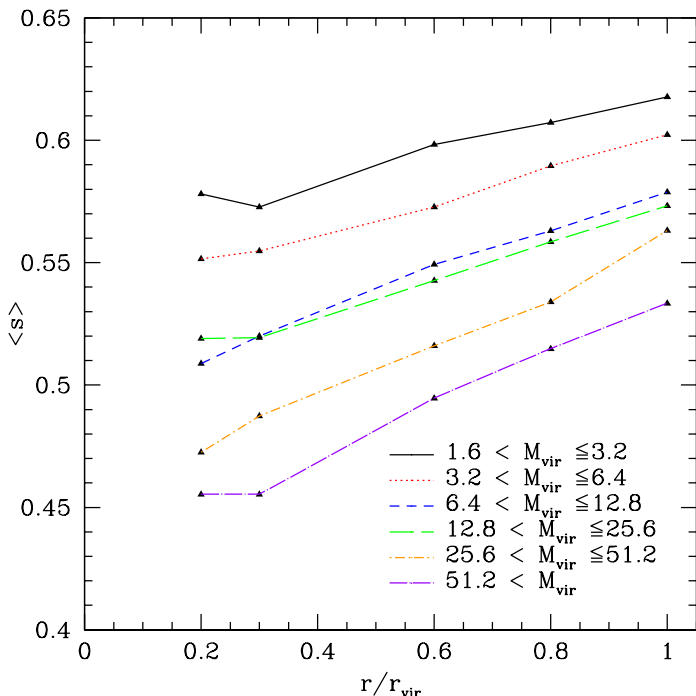


Figure 7. $\langle s \rangle$ as a function of radius at $z = 0$.

mass halos. In order to study the radial dependence of shape, halos in the $L80_{0.9b}$ simulation were examined at 5 different fractions of their virial radius (Figure 7). For all halo mass bins there is a tendency for halos to be more spherical at larger radii, with more massive halos having a steeper change in $\langle s \rangle$ with radius.

We also examined the value of $\langle p \rangle$ with radius and found no radial dependence. Therefore, a and b have the same radial dependence and the largest axis a becomes relatively shorter with radius. We examine the relationship of the radial dependence of s with mass and combine it with Equation (7) to find a shape-radius relationship,

$$\langle s \rangle(M_{\text{vir}}, r) = b(M_{\text{vir}})(r/r_{\text{vir}} - 0.3) + 0.54(M_{\text{vir}}/M_*)^{-0.05} \quad (10)$$

with

$$b(M_{\text{vir}}) = 0.037 \log_{10}(M_{\text{vir}}/M_*) + 0.062. \quad (11)$$

We also examined the shape at different radii with a spherical window. The shape of the halo did not change very much on average with radius. This is consistent with the result of Bailin & Steinmetz (2005) (see Section 6).

4.7 Triaxiality

Often ellipsoids are described in terms of their triaxiality (prolate, oblate, or triaxial). One way of expressing the triaxiality of an ellipsoid is by using the triaxiality parameter Franx, Illingworth & de Zeeuw (1991):

$$T \equiv \frac{a^2 - b^2}{a^2 - c^2} = \frac{1 - q^2}{1 - s^2}. \quad (12)$$

An ellipsoid is considered *oblate* if $0 < T < 1/3$, *triaxial* with $1/3 < T < 2/3$, and *prolate* if $2/3 < T < 1$. In Figure 8 we divide up the halos into the same mass bins as in Figure 7 and analyse the triaxiality at $R = 0.3R_{\text{vir}}$ and R_{vir} . We find that most halos are prolate in shape with very few oblate halos, even at R_{vir} . The deficit of halos with T very close to 1 is not physical. Due to the iterative process we use to define shapes, if any two of the axes become degenerate (same length) the process has trouble converging. In most cases it does converge but with a large systematic error. Some authors have suggested that halos become oblate at large radii. We find only a small trend to less prolateness at large radii, but no evidence of a shift to oblate. Figure 8 also shows that larger halos, mainly those above M_* , are almost entirely prolate. Because we expect halos with masses above M_* to be undergoing a higher rate of merging than halos with masses below M_* , and because it has been shown that this merging happens along preferred directions (Knebe et al. 2004; Zentner et al. 2005b; Faltenbacher et al. 2005), the prolateness is most likely due to merging. This is in support of the idea that halo merging is responsible for the distribution of shapes. The internal velocity of a halo is also related to the merger history and therefore one would expect a relationship between the velocity structure of halos and their shape. We examine this in the next subsection.

4.8 Alignment with Velocity and Angular Momentum

We have shown that the shape of a halo is related to the mass and have seen some clues that the shape is due to merging.

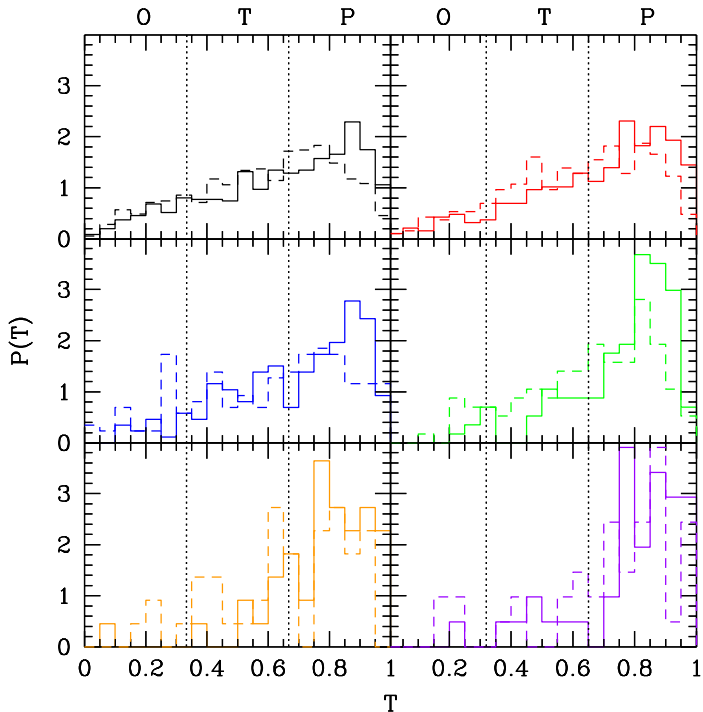


Figure 8. Triaxiality of halos at $z = 0$ at $R = 0.3R_{\text{vir}}$ (solid) and R_{vir} (dashed). Beginning with the top left histogram and moving right, then down, the triaxiality of halos is divided into the same mass bins as in Figure 7.

Merging is also related to the angular momentum of halos (Vitvitska et al. 2002) and their velocity dispersion. In order for a collisionless system such as a DM halo to sustain its shape after merging, there must be an internal pressure provided by the velocity dispersion. If this is the case one would expect the internal velocities to be correlated with the shape. In order to investigate this we examine the alignment of the angular momentum and the velocity anisotropy of the halo with the shape. The angular momentum used here is calculated using the same particles found in the final ellipsoidal volume from our iterative method for determining the shape, although the results do not have a large dependence on which subset of particles within the halo is used. We find, as was pointed out by Warren et al. (1992), Tormen (1997), and subsequently seen by others, that the angular momentum is highly correlated with the smallest axis of the halo. In Figure 9 we show the absolute cosine of the angle between the indicated axis and the angular momentum vector. If the orientations were random the plot would be of a straight line at a value of 0.5. A peak at $|\cos\theta| = 1$ means that the axes are most often aligned and a peak at $|\cos\theta| = 0$ means that the axes are most often perpendicular to the angular momentum. As one can see, the smallest axis is most often aligned and the largest axis is most often at an angle of $\pi/2$ from the angular momentum. Although the angular momentum is aligned with the smallest axis as would be expected for an object which is rotationally supported, DM halos are found not to be rotationally supported. Therefore, the significance of this alignment points not to a cause and effect relationship but to a shared origin. It has been shown in previous studies that the angular momentum of halos is

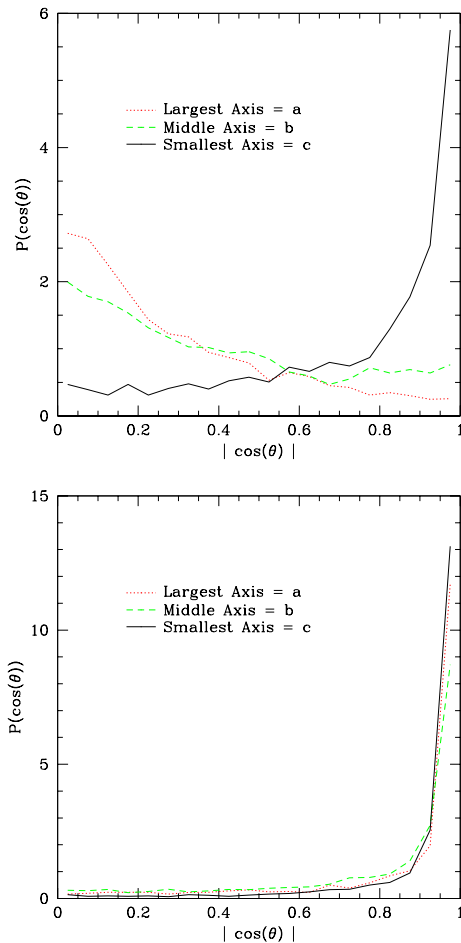


Figure 9. Top: The probability distribution of the cosine of the angles between the largest, middle, and smallest axis and the angular momentum vector. If the angular momentum were randomly oriented the graph would be a flat line at a value of 0.5. Bottom: The probability distribution of the cosine of the angles between the shape axes and velocity anisotropy axes. The velocity anisotropy is highly correlated with the shape.

largely determined by the last major merger (Vitvitska et al. 2002), and that, at least during very active periods, merging (both minor and major) happens along preferred directions (Knebe et al. 2004; Zentner et al. 2005b; Faltenbacher et al. 2005). It would seem, based on this, that the shapes and orientations of DM halos, at least during active merging periods, can be attributed to directional merging.

In order to determine whether halos are relaxed and self supporting we examine the relation of the velocity anisotropy to the shapes of halos. The velocity anisotropy is defined in the same way as the inertia tensor used to measure the shape,

$$V_{ij} \equiv \sum_n v_{i,n} v_{j,n}. \quad (13)$$

We do not use a weighted version of this and we do not iterate, because neither of these make much physical sense. We calculate the velocity anisotropy tensor again using the particles found within the ellipsoidal shell defined by the shape analysis. As with the angular momentum the alignment is

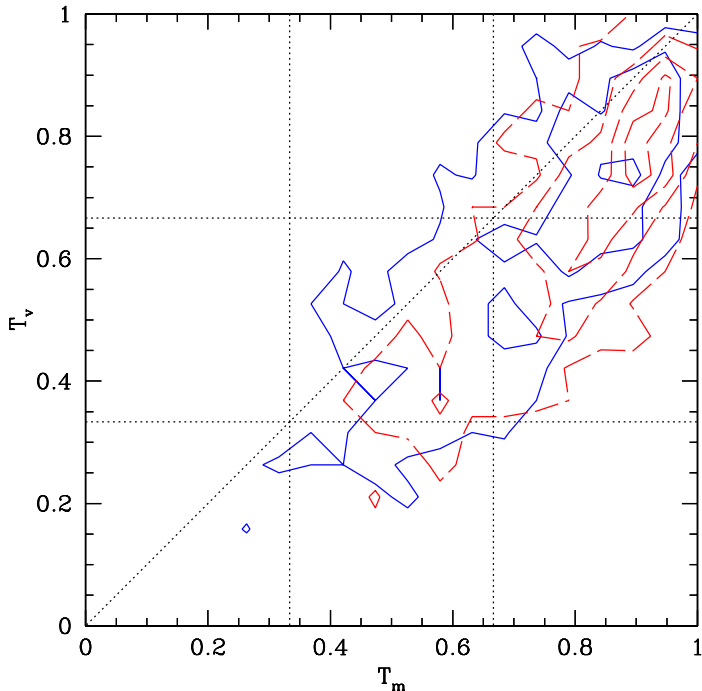


Figure 10. Triaxiality of the velocity anisotropy tensor and the shape for $R = 0.3R_{\text{vir}}$ (blue) and R_{vir} (red).

very insensitive to the particles used. We then determine the angle between the respective axis (i.e. a , b , & c). In Figure 9 we plot the distribution of absolute cosines between a_{shape} and a_{vel} , b_{shape} and b_{vel} , and c_{shape} and c_{vel} . From this one can see that all three of the axes are highly correlated. The strength of the alignment between the velocity anisotropy tensor and the shape suggests that the shape is supported by internal velocities. But how does the shape relate more directly to the velocity anisotropy?

In Figure 10 we show the triaxiality of the velocity anisotropy and the density. The velocity anisotropy on average is more spherical in shape than the density. This is the expected trend from the Jeans equation for an ellipsoidal distribution. The velocity anisotropy is directly related to the potential which has the same orientation as the shape but is more spherical due to the fact that potential is related to the spacial derivative of the density. It would therefore seem that the mass dependence of shape can not be explained by different relaxation times. This is also supported by the fact that halos are more aspherical in the centre where the relaxation time would be shorter than at the virial radius.

5 MERGER HISTORY AND SHAPES

So far we have investigated the evolution of halo shapes in fixed mass bins as a function of redshift and for two different values of σ_8 . Additional insight into the origin of shapes and their dispersion can be gained by tracing the evolution of individual halos. In order to quantify the evolution or mass accretion history (MAH) of the halos we have constructed merger trees. For more information on the merger trees, please see Allgood (2005). From these merger trees

we determine the MAH for each halo at $z = 0$ by following the evolution of its most massive progenitors. Wechsler et al. (2002) showed that the MAH of a halo can usually be well fit by a single parameter model,

$$M(a) = M_o \exp \left[-2a_c \left(\frac{1}{a} - 1 \right) \right], \quad (14)$$

where M_o is the mass of the halo at $z = 0$ and a_c is the scale factor at which the log slope of the MAH is 2. Although in the Wechsler et al. (2002) they only allowed a_c to be a free parameter, we find that by also allowing M_o to be a free parameter we are able to better recover a_c for halos which had experienced a recent major merger. Halos with lower values of a_c formed earlier, and as shown by Wechsler et al. (2002), have a higher concentration. By means of Equation (14) we assign an a_c to every halo found at $z = 0$.

In Figure 11 we plot s versus a_c for the halos in the L120_{0.9} simulation split into separate mass bins. We find that halos which formed earlier are on average more spherical with a dispersion of 0.08–0.1 (see Figure 12) for all mass bins. This implies that the scatter in the $\langle s \rangle(M_{\text{vir}})$ relation can not be completely attributed to the different values of a_c for that particular mass bin. However, the dependence on a_c is less for the higher mass halos and this would explain the mean-dispersion relationship explored in Subsection 4.4. Higher mass halos were found to have a smaller dispersion than lower mass halos at $z = 0$. This can also be seen in Figure 12. It is very likely that the residual scatter is due, at least in part, to the pattern of infall. Since s is derived from an inherently three dimensional quantity, namely the inertial tensor, a one dimension parameterisation may not be sufficient to capture all of the physics involved. A more careful study of infall is needed to explain the dispersion in s .

The above investigation makes clear that the dispersion of halo shapes cannot be explained by appealing to a single parameter description of the MAHs. However, an average evolutionary pattern for halos which is dependent on both a_c and mass is seen. Figure 13 displays the evolution of $\langle s \rangle$ (sorted by a_c) with scale factor a for a particular mass bin at $z = 0$. Halos that formed early (lower a_c) are more spherical today as was pointed out above. Moreover, they become spherical more rapidly (indicated by the increasing slopes for halos of low a_c), although the transformation rate towards spherical shapes seems to slow for all values of a_c with increasing expansion factor. In Figure 13 the results for the lowest mass bin ($3.2 \times 10^{12} < M_{\text{vir}} < 6.4 \times 10^{12}$) are shown. Apart from a systematic shift to lower values of s the corresponding plots for higher mass bins look very similar.

Halos which have early formation times (low a_c) at a fixed mass today have typically accreted more mass since a_c than halos with higher values of a_c . The rapid transformation towards spherical shapes for early forming halos implies either that lower mass halos become spherical more rapidly after a_c , probably due to shorter dynamical times, or that mass accretion after a_c is more spherical, therefore causing the halo to become more spherical as well. By examining other mass bins we find that halos of different masses today but with comparable values for a_c , thus different masses at a_c , show the same rate of change in s , but with different initial values of s . This finding suggests that the rate at which a halo becomes spherical depends on its a_c rather than on

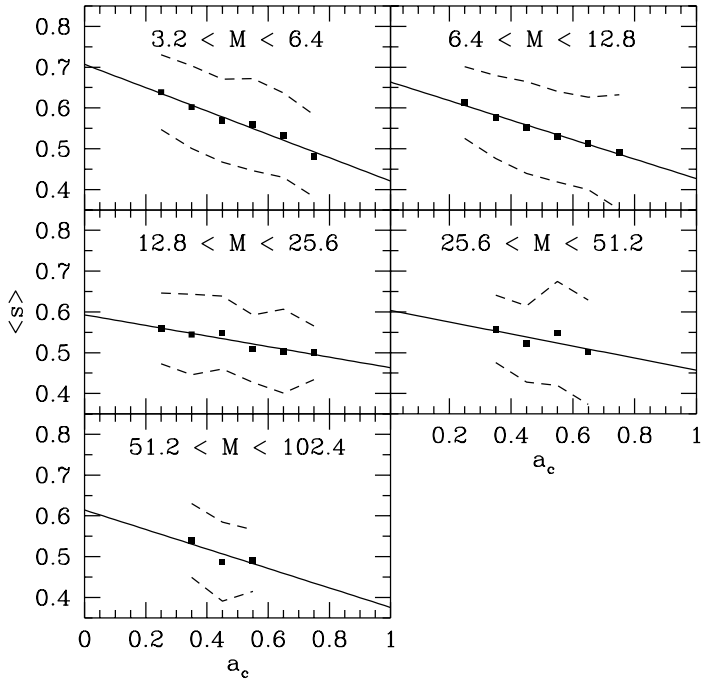


Figure 11. $\langle s \rangle$ vs characteristic formation epoch for different mass bins (mass quoted in units of $10^{12}h^{-1} M_{\odot}$). Only bins that contain at least 10 halos are shown (square points). There is a distinct trend of shape with a_c for the lower mass bins. At higher mass there is still a trend but it is uncertain how strong the trend is due to the lower number statistics. Solid black line is a linear fit to the points and dashed line is the 1σ scatter about the points.

its mass. We find that we can approximate the dependence of s on the expansion factor a for $a > a_c + 0.1$ by a simple power law

$$\langle s \rangle(a) \propto (a - a_c)^{\nu} : a > a_c + 0.1, \quad (15)$$

where ν has to be fitted for the particular halo. In Figure 14 we display the values of ν versus a_c determined by χ^2 fitting for the L80_{0.9b} simulation. The L80_{0.9b} was divided into bins of log mass and a_c . The average MAH for each bin was fit by Equation (15) using χ^2 minimisation. All bins containing at least 20 halos were used to determine the function ν . We find a tight correlation between the ν and a_c which can be approximated by

$$\nu = 1.74 \times a_c^{-0.3}. \quad (16)$$

This fit is represented by the solid line in Figure 14. The remarkable success of Equation (15) to fit the data supports the idea, that the transformation from aspherical to spherical halo shapes is driven by mass accretion becoming more spherical after a_c . The physical reason for the observed behaviour merits further investigation.

6 COMPARISON WITH PREVIOUS DETERMINATIONS OF HALO SHAPE

In the previous sections we have explored many aspects of halo shapes. Central to this discussion has been $\langle s \rangle(M_{\text{vir}})$.

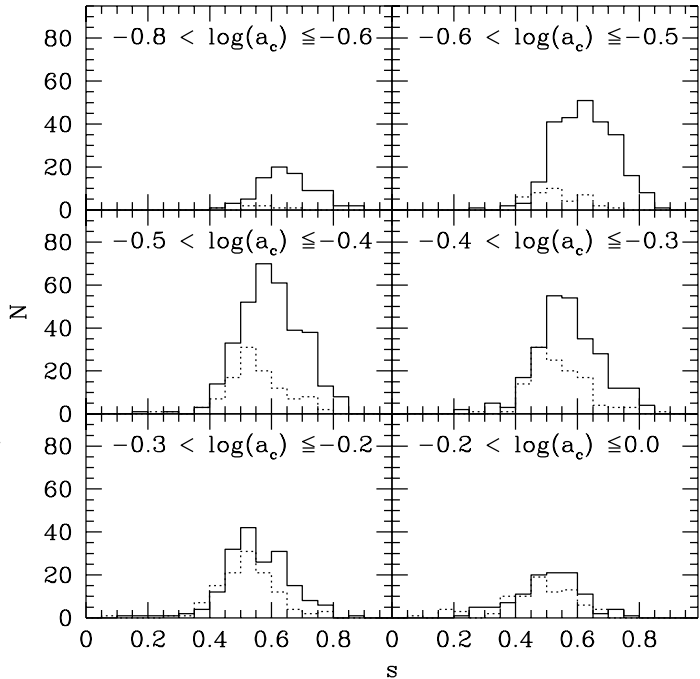


Figure 12. Distributions of s for a given range in a_c and mass. The solid histogram is for the mass range: $3.2 \times 10^{12} < M_{\text{vir}} < 6.4 \times 10^{12}$ and the dotted histogram is for a mass range of $1.28 \times 10^{13} < M_{\text{vir}} < 5.12 \times 10^{13}$. The dispersion in s in a given mass bin can be explained in part by the different MAHs.

This relationship has been examined by many recent studies all of which seem to determine different relationships. In this section we address these discrepancies.

First, an examination of the difference in the inferred shape from the use of the weighted versus the unweighted inertia tensor is needed. Most recent authors prefer the weighted (or reduced) inertia tensor (Equation (5)) which is the method we have chosen to use. The motivation for the use of the weighted inertia tensor, \tilde{I} , is due to the bias present in the unweighted method to particles at larger radii. By weighting the contribution from each particle in the sum by the distance to the particle squared, \tilde{I} is less sensitive to large substructure in the outer regions of the analysis volume. To test the difference between the methods we examined a sample of halos from the L120_{0.9} simulation using the iterative method with both versions of inertia tensor (Figure 15). Both iterative methods give similar results for the mean quantities (inset in Figure 15) as a function of mass with individual halos differing by $\Delta s \leq 0.15$. The detailed distributions are different and have some interesting features (Table 3). We find that halos which have lower s values for the weighted method over the unweighted method have larger substructure near the centre and halos which have lower s values for the unweighted method had larger substructure near the outer edge of the analysis volume. At very small axial ratios the unweighted method seems to always give larger axial ratios. As we have shown, halos with $s \lesssim 0.3$ are late forming and are strongly contaminated by substructure. This leads to the unweighted method giving a lower value of s indicated by the high skewness shown for the method

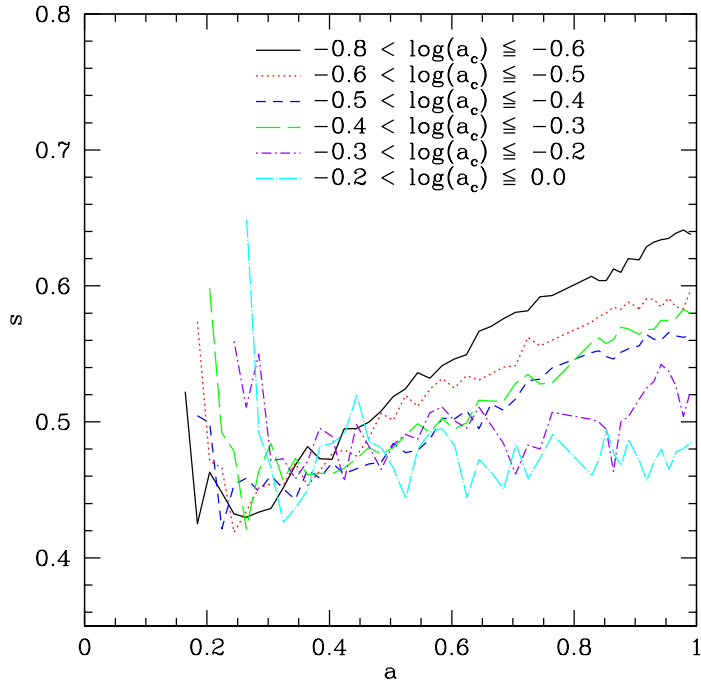


Figure 13. The evolution of halos with different values of a_c in the mass bin $3.2 \times 10^{12} < M_{\text{vir}}(z=0) < 6.4 \times 10^{12}$. Halos become more spherical after a short period after a_c . The halos which form earlier become spherical more rapidly. Log binning was chosen to even out the number of halos in each bin.

Table 3. Weighted vs. Unweighted Shapes

Method	Mean Mass	$\langle s \rangle$	σ_s	kurtosis	skewness
weighted	5×10^{11}	0.694	0.094	-0.029	-0.132
unweighted	5×10^{11}	0.686	0.097	-0.302	-0.053
weighted	5×10^{12}	0.614	0.111	0.253	-0.188
unweighted	5×10^{12}	0.603	0.118	0.605	-0.287
weighted	5×10^{13}	0.518	0.117	1.756	-0.532
unweighted	5×10^{13}	0.524	0.126	1.628	-0.592
weighted	5×10^{14}	0.455	0.114	2.066	-0.515
unweighted	5×10^{14}	0.472	0.133	1.428	0.150

in Table 3 by the skewness. For the two well resolved mass ranges ($10^{12} < M_{\text{vir}} < 10^{13}$ and $10^{13} < M_{\text{vir}} < 10^{14}$) the unweighted method has a larger negative skewness. Note that all mass bins except for the last unweighted bin have negative skewness (this was discussed in Section 4), but the most massive bin suffers from low statistics. The distribution of σ_s values is always broader for the unweighted method.

There are more differences than just the form of the inertia tensor used. In order to compare our results to a selected number of previous results (Figure 16) we have repeated the shape analysis using the methods described in the corresponding papers. The previous work which is most similar to the current work is that of Springel et al. (2004).

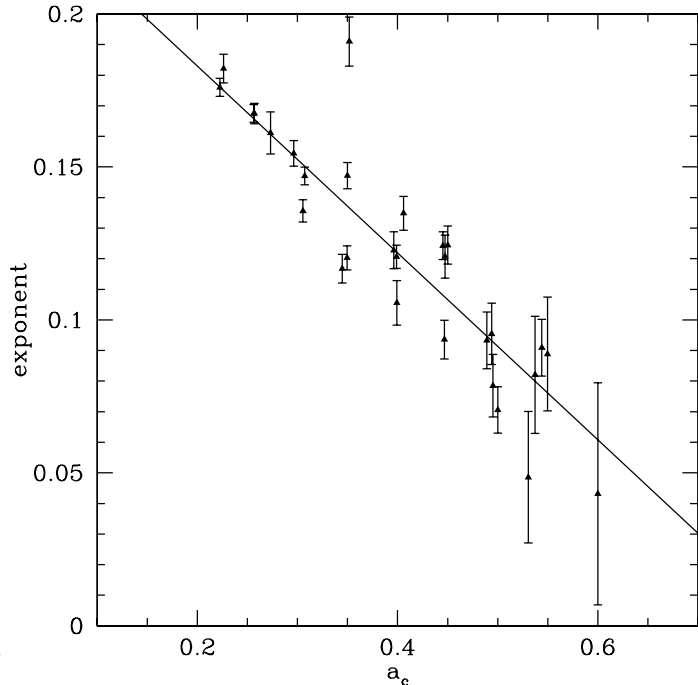


Figure 14. The rate of change exponent ν (see Equation (15)) versus expansion factor at halo formation a_c . The solid line displays the fitting formula given by Equation (16). Only bins containing at least 20 halos is displayed. The a_c value of each point is the average value for that respective bin and the errorbars represent the variance determined by the χ^2 fitting.

Our findings are very similar to the Springel et al. (2004) results except we found that $\langle s \rangle(M_{\text{vir}})$ has a slightly higher normalisation. Through private communication with Volker Springel, we were provided with an updated set of data points which come from a more complete sample and are in much better agreement with our results (open green squares in Figure 16). Not only do our results agree at $z=0$, but also at higher redshift (see Figure 2).

Jing & Suto (2002) (JS) studied 12 high resolution clusters with $N \sim 10^6$ particles and five cosmological simulations with $N = 512^3$ particles in a $100h^{-1}$ Mpc box with both an SCDM and Λ CDM cosmology. The simulations were performed with a P³M code with fixed timestepping and a spatial resolution of $10 - 20h^{-1}$ kpc. They used a FOF halo finder and analysed the shapes of the high resolution clusters in isodensity shells as a function of radius, finding that the halos are more spherical at larger radii. After determining the relationship of shape with radius they developed a generalised ellipsoidal NFW density profile (Figure 17 shows that our method gives similar results). They applied this generalised fitting routine to the cosmological simulations and determined generalised NFW parameters and shapes statistics. The shapes were determined using an isodensity shell at an over density of $2500\rho_c$ (where ρ_c is the critical density) which corresponds roughly to $R = 0.3R_{\text{vir}}$. The mass range analysed only covered one order of magnitude in mass ($2.1 \times 10^{13}h^{-1} M_{\odot} \leq M_{\text{vir}} \lesssim 1 \times 10^{14}h^{-1} M_{\odot}$). They found a result very similar to ours, $\langle s \rangle(M_{\text{vir}}) = 0.54(M_{\text{vir}}/M_*)^{-0.07[\Omega_m(z)]^{0.7}}$, and

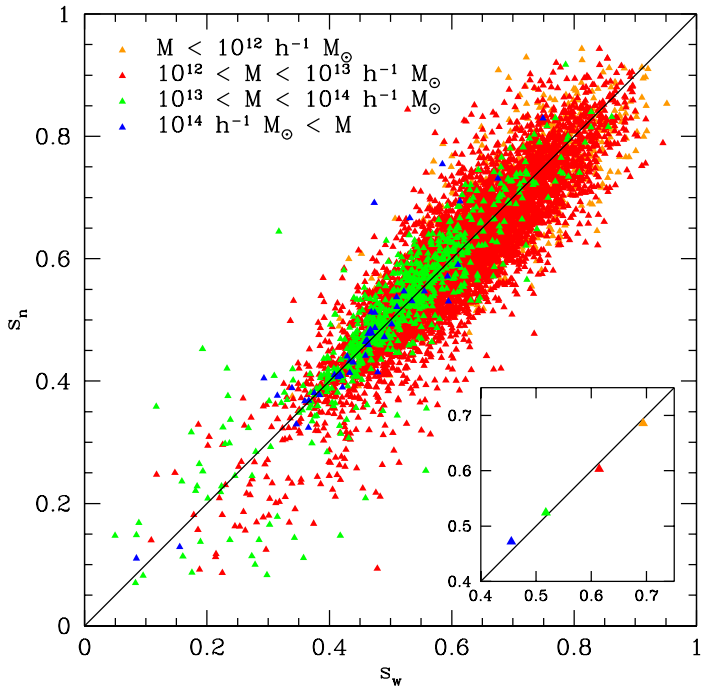


Figure 15. Axial ratios for halos in a cosmological simulation are divided into mass bins and the shapes are calculated using the weighted (s_w) and non-weighted (s_n) iterative inertia tensor methods. The two methods agree within $\sim 10\%$ and give the same value when averaged over a given mass bin (inset graph).

dispersion which is well fit by a Gaussian distribution with $\sigma_s(M_{\text{vir}}) = 0.113(M_{\text{vir}}/M_*)^{-0.07[\Omega_m(z)]^{0.7}}$. We do not find any evidence for a steepening of the exponent with redshift as they do.

The disagreement between our findings and those of JS regarding the scaling of $\langle s \rangle$ with mass is due to the procedures used. In the JS analysis they determine the shape of an isodensity shell at $2500\rho_c \pm 3\%$, completely ignoring the interior of the shell. JS analysed halos with masses greater than $6.2 \times 10^{12} h^{-1} M_\odot$ which tend to be dynamically young and often have double cores. This can affect the shape a lot, but their analysis would not pick this up, due to the neglect of the central region. In our iterative inertia tensor analysis we include the centres. In order to confirm that the difference is truly due to the shell versus the solid ellipsoid we analysed halos from the L200_{0.9} simulation in the mass range $1 - 4 \times 10^{14} h^{-1} M_\odot$ using the technique presented in JS. We examined isodensity shells at $2500\rho_c$ with a thickness of $\pm 30\%$, instead of the $\pm 3\%$ used by JS. We needed to examine thicker shells in order to obtain enough particles to do the analysis because the L200_{0.9} has less mass resolution than the simulations studied by JS. We found that the inertia tensor method gives $\langle s \rangle_{\text{tensor}} = 0.485 \pm 0.008$ and $\sigma_s = 0.091 \pm 0.006$ and the JS method gives $\langle s \rangle_{\text{JS}} = 0.515 \pm 0.008$ with the same scatter for the same halos. The difference is due to the fact that s_{JS} is systematically larger at low s_{tensor} . This pattern is born out by a quantitative analysis. When we split the sample at $s_{\text{tensor}} = 0.45$ (roughly where agreement begins), we get that above $s_{\text{tensor}} = 0.45$ the samples agree quite well with

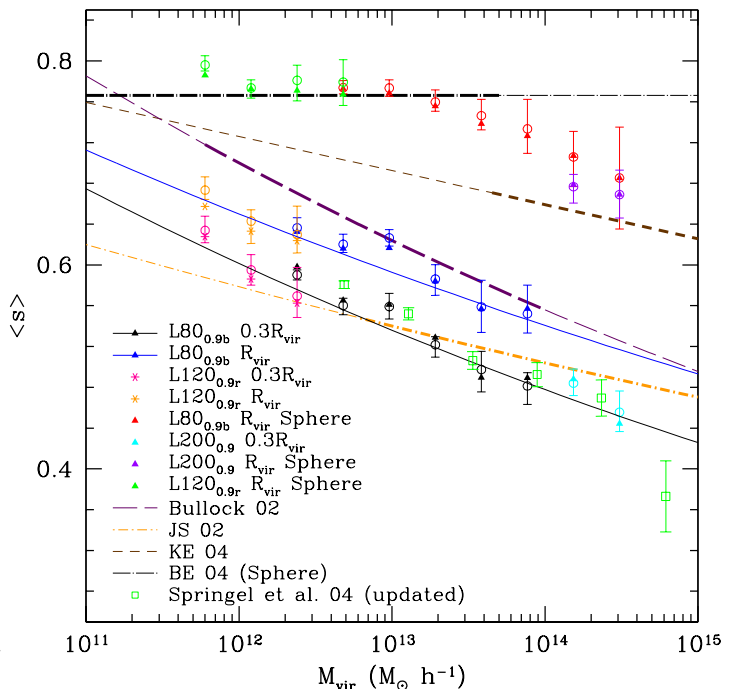


Figure 16. Comparison of $\langle s \rangle(M_{\text{vir}})$ relation with previous studies. We attempt to reconcile the differences between our results and those of other authors. We present the results of a shape analysis of the L80_{0.9b}, L120_{0.90r}, and L200_{0.9} simulations using the iterative inertia methods at $R = 0.3R_{\text{vir}}$ (black,pink,cyan) and non-iterative spherical window analysis at R_{vir} (red,green,violet). In addition, we present the results of a shape analysis of the L80_{0.9b} and L120_{0.90r} using the iterative method at R_{vir} (blue). The black line is our proposed fit from Equation (7) and this should be compared to the results of Springel (private communication) (green open squares) and Jing & Suto (2002) (orange dot dash). The blue line is a fit to the blue points, which should be compared to the Bullock (2002) line (violet long dash). Finally the red line is a renormalised version of the Kasun & Evrard (2004) fit which should be compared their fit (brown small dash). The thin black dot dash line at $\langle s \rangle \sim 0.7$ is the spherical shell fit of Bailin & Steinmetz (2005). The bold portions of the lines indicate the mass ranges where the fit was compared to simulated data by the respective authors.

$\langle s \rangle_{\text{tensor}} = 0.571 \pm 0.007$ vs $\langle s \rangle_{\text{JS}} = 0.576 \pm 0.011$. Whereas below $s_{\text{tensor}} = 0.45$ we get $\langle s \rangle_{\text{tensor}} = 0.424 \pm 0.007$ vs $\langle s \rangle_{\text{JS}} = 0.472 \pm 0.008$. The difference at the low end is due to the missing of the dynamically active cores by JS. If JS had extended their analysis to lower mass halos were multiple cores are not as common their determination of $\langle s \rangle$ would converge with ours. Because X-ray observers normally do not choose to only analyse the outer shells of clusters due to the fact that the X-ray observations get noisier with the distance from the centre and because optical observers may not see the multiple cores when analysing cluster member velocities, we prefer the method which includes the effect of the multiple peaks. In Paper II we show that using our method with some additional assumptions one can account for the observed X-ray ellipticity measurements.

Bullock (2002) analysed the shapes of halos in a Λ CDM simulation with $\sigma_8 = 1.0$ at three different redshifts ($z =$

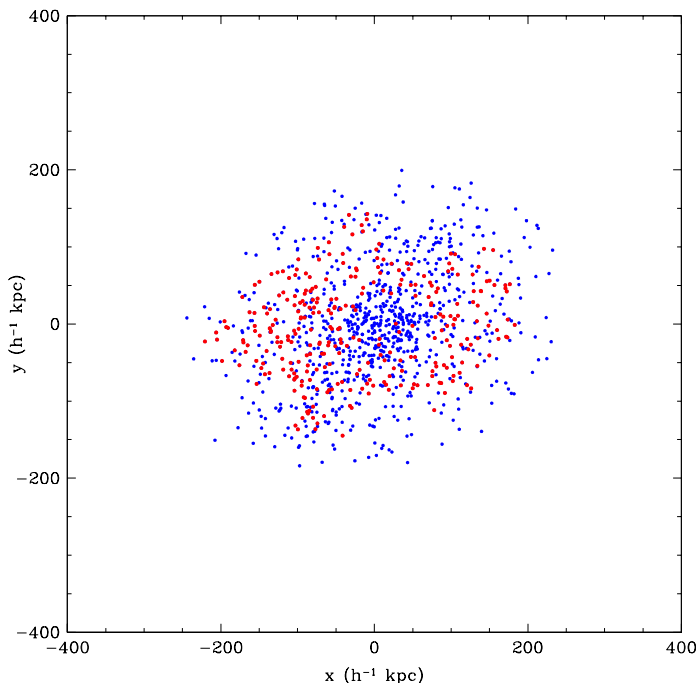


Figure 17. Comparison of an isodensity shell (red) and a tensor ellipsoid (blue). Particles are selected by the JS (red) and inertia tensor (blue) methods and projected on the x - y plane of the simulation box. The shortest/longest axis ratio is $s = 0.49$ (0.48) for the isodensity shell (tensor ellipsoid). The semi-major axis of the isodensity shell $0.23R_{\text{vir}}$, consistent with JS for $2500\rho_c$ isodensity.

0.0, 1.0, 3.0). The simulations were performed using the ART code in a $60h^{-1}$ Mpc box with 256^3 particles and spatial resolution of $1.8h^{-1}$ kpc. The analysis of shape was done using the weighted inertia tensor in a spherical window with $R = R_{\text{vir}}$. The axial ratios were determined iteratively until convergence was obtained using a similar criterion as we have used, but the window remained spherical. The use of the weighted inertia tensor and iterative axial ratio determination seemed to almost eliminate the effect of using a spherical window (discussed below). Bullock (2002) found that $\langle s \rangle (M_{\text{vir}}) \simeq 0.7 (M_{\text{vir}}/10^{12} h^{-1} M_{\odot})^{-0.05} (1+z)^{-0.2}$ was a good fit to the simulation. The empirical scaling of Bullock (2002) is similar to what we find, but the powerlaw is steeper. This can be attributed to the lower resolution and possibly the use of a spherical window. Bullock’s higher normalisation is due to the higher σ_8 .

Kasun & Evrard (2004) determined the shapes of cluster halos ($M_{200} > 3 \times 10^{14} h^{-1} M_{\odot}$) in the Hubble Volume simulation. They calculated the axial ratios using the unweighted inertia tensor in a spherical window at R_{200} , the radius of the sphere within which the mean density is $200\rho_c(z)$, with $\rho_c(z)$ being the critical density at redshift z . They determined a relationship of $\langle s \rangle (M_{\text{vir}}) = 0.631 [1 - 0.023 \ln(M_{\text{vir}}/10^{15} h^{-1} M_{\odot})] (1+z)^{-0.086}$. We compare our analysis with theirs by performing the same spherical analysis at $R = R_{\text{vir}}$, which is slightly larger than R_{200} . We find that in our largest box simulation (L200_{0.9}) where we have good statistics on cluster mass halos we find good

agreement. In examining the other two simulations for lower mass halos we are unable to recover the extrapolation of the Kasun & Evrard (2004) relationship. In fact, we see a transition from the Kasun & Evrard (2004) relationship to the relationship of Bailin & Steinmetz (2005) (discussed below). We also find that the mean shape relationship has almost no dependence on radius when using a spherical window function.

Bailin & Steinmetz (2005) analyse the shapes of halos at different radii in spherical shells in the mass range of $10^{11} h^{-1} M_{\odot} < M \lesssim 5 \times 10^{13}$. After determining the axial ratios they then apply an empirical correction of $s_{\text{true}} = s_{\text{measure}}^{\sqrt{3}}$ to correct for the use of a spherical window. They find that all halos have an axial ratio of $\langle s \rangle \sim 0.63$ at $R = 0.4R_{\text{vir}}$ with the scaling applied, which implies that they measure $\langle s \rangle \sim 0.766$ in their spherical window. This result is in very good agreement with our spherical analysis (green and red data points in Figure 16). However, we do not find that halos of different masses have the same mean axial ratio. There seems to be some evidence that the $\langle s \rangle (M_{\text{vir}})$ relationship flattens out below M_* , but it is definitely not constant with radius. Simulations with even higher mass resolution are needed to investigate for the possibility of flattening below M_* . For an extra check we also analysed the halos in a spherical shell between $0.25R_{\text{vir}}$ and $0.4R_{\text{vir}}$ and measure a roughly flat value for all halos of $s = 0.77$. The disagreement about the $\langle s \rangle (M)$ relationship most likely lies in the determination of the empirical spherical window correction. The correction was determined using Monte Carlo halos with no substructure, but we find that substructure plays a role in the determined shape of the halo.

7 COMPARISON WITH OBSERVATIONS

Since all of the differences between the shape statistics extracted from pure collisionless simulations by various authors can be reconciled by considering the different methods used to determine shapes, a comparison between observations and simulations is in order. Much of the attention halo shapes have received lately is due to the recent estimates of the shape of the Milky Way’s host halo. Most estimates find the Milky Way’s host halo to have an oblate shape with $s \geq 0.8$. This is in contrast with $s \approx 0.6 \pm 0.1$ for $10^{12} h^{-1} M_{\odot}$ halos found in pure collisionless simulations, though there is some evidence that the halos become more spherical when baryonic cooling is included (Kazantzidis et al. 2004; Bailin et al. 2005) and that some become oblate. The presence of gas cooling will invariably make the halos more spherical but the extent of the effect is not yet fully understood. Recently, there have however been studies of the M giants in the leading edge of the Sagittarius dwarf stream (Helmi 2004; Law et al. 2005), which concluded that the best fit shape of the host halo is a prolate ellipsoid with $s = 0.6$.

Another way of measuring the shape of DM halos is through weak lensing. Hoekstra et al. (2004) and Mandelbaum et al. (2005) performed studies of galaxy-galaxy weak lensing using the Red-Sequence Cluster Survey and the Sloan Digital Sky Survey respectively. Hoekstra et al. (2004) determine the average shapes of halos by measuring the orientation of the galaxies, then stacking

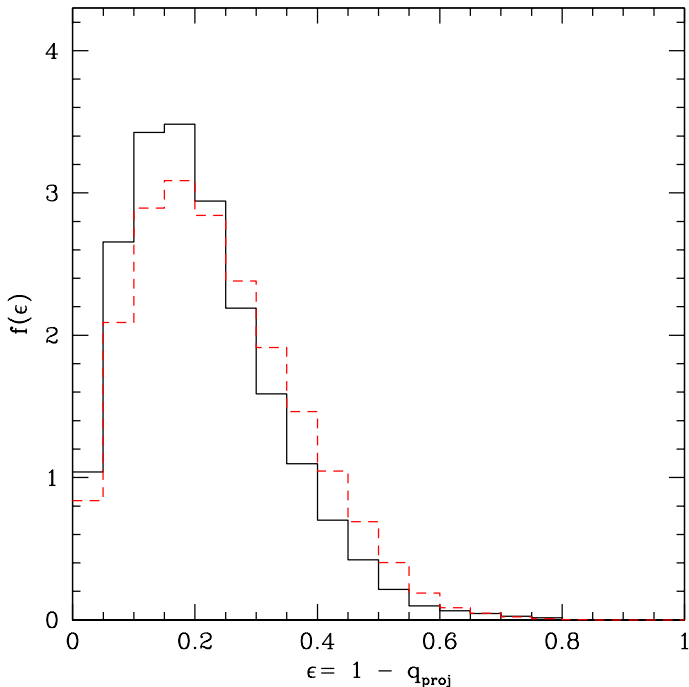


Figure 18. Projected ellipticity of galaxy mass halos at $z = 0.33$ for $\sigma_8 = 0.9$ (black solid) and $\sigma_8 = 0.75$ (red dashed).

the galaxy images with the orientations aligned, and finally measuring the shear field around the stacked image. This measurement of the shear provides a rough estimate of the dark matter halo shapes at $z \approx 0.33$. They found an average projected ellipticity of $\langle \epsilon \rangle \equiv \langle 1 - q_{2D} \rangle = 0.20^{+0.04}_{-0.05}$, corresponding to $s = 0.66^{+0.07}_{-0.06}$, for halos with an average mass of $8 \times 10^{11} h^{-1} M_{\odot}$. The Hoekstra et al. (2004) determination was hindered by the fact that the galaxies were stacked together regardless of morphological type, and one would reasonably assume that morphological type is related to merger history and possibly orientation with the host halo which will in turn affect the measured halo shapes as we have shown.

In the Mandelbaum et al. (2005) analysis of SDSS galaxies colour was used as a proxy for morphological type. Mandelbaum et al. (2005) studied 2 million lens galaxies with $r > 19$ and 31 million source galaxies dividing the lenses into bins of colour and luminosity. They find a suggestion that spiral (blue galaxy) light ellipticities may be anti-aligned with the halo ellipticities at the 2σ level and a suggestion that elliptical (red galaxy) host halo ellipticities are luminosity dependent. Since we and others have shown that halo angular momentum is highly aligned with the smallest axis, this finding would suggest that the angular momentum of spiral galaxies is not aligned with the angular momentum of their host halos. Recent theoretical work by Bailin et al. (2005) seems to support this idea as well, although they only study eight spiral galaxy simulations. If this were the case one would assume that in the Hoekstra et al. (2004) analysis the measured signal would be diminished by this. It would not be completely nullified because the Hoekstra et al. (2004) sample is dominated by elliptical galaxies. Indeed, Mandelbaum et al. (2005) show by

combining the appropriate luminosity and colour bins that their findings are in agreement with those of Hoekstra et al. (2004). In Figure 18 we have plotted the distribution of projected axial ratios for the L80_{0.9a} and L80_{0.75} simulations for 1000 random lines of sight through the box for galaxy mass halos. In projection the differences between the simulations become small hindering any sort of determination of σ_8 via lensing studies. The peaks of the distributions are both broadly in agreement with the findings of Hoekstra et al. (2004) and Mandelbaum et al. (2005). Further study of the galaxy / host halo alignment relationship and galaxy morphology / halo merger history relationship is in order to better understand and predict the galaxy-galaxy lensing measurements.

8 SUMMARY AND DISCUSSION

First we investigated the dependence of halo shapes on their masses. Our halo sample, based on six different simulations, covers three orders of magnitude in mass from galaxy to cluster scales. Furthermore we have examined halo shapes as a function of redshift and σ_8 . Our analysis of shape is based on the halo volume enclosed by $R \approx 0.3R_{\text{vir}}$. This particular radius is chosen for several reasons; halos should be fairly well relaxed within this radius and shapes measured from X-ray gas in cluster should extend to this radius. At this and other radii we find that the mean shape of dark matter halos depends on the halos mass. We find that the mean largest-to-smallest axial ratio $s = c/a$ at radius $0.3R_{\text{vir}}$ is well described by

$$\langle s \rangle(M_{\text{vir}}, z) = (0.54 \pm 0.03) \left(\frac{M_{\text{vir}}}{M_*(z)} \right)^{-0.050 \pm 0.003} \quad (17)$$

The distribution of s in each mass bin is well fit by a Gaussian with $\sigma = 0.1$. The relation found here is steeper than that of Jing & Suto (2002) at $z = 0$, thus predicting less spherical cluster mass halos and more spherical galaxy mass halos.

In order to reconcile our results with sometimes strongly deviating findings by other authors we have applied their particular methods. We find that the disagreements between different studies are mostly due to differences between methods of measuring axial ratios. However, there remains one open question brought up by this comparison. There seems to be an inconsistency between the analysis by Kasun & Evrard (2004), if extended to galaxy mass halos, and Bailin & Steinmetz (2005). Both groups analysed halo shapes within a spherical window. We find that the application of a spherical window leads to a transition from a power-law like behaviour above M_* to a mass independent shape below M_* . This transition is found in the gap between the mass ranges analysed by the two groups and therefore was not recognised by either of them. Possibly a similar transition can be found applying our method of an iterative ellipsoidal window. But the effect seems to be smaller and requires, if apparent, even higher mass resolution than utilised in this work.

We find that the mean shape relation becomes shallower and more spherical at increased radius. We also find that higher mass halos have a steeper relationship between shape and radius than smaller mass halos. Since cluster sized

halos are on average younger than galaxy sized halos, we are comparing dynamically different objects. The presence of an increased amount of massive substructure near the centre of dynamically young objects may be the reason for the steeper relation of shape with radius for cluster mass halos than galaxy mass halos.

Our analysis of the halo shapes as a function of redshift leads to the following results. Within fixed mass bins the redshift dependence of $\langle s \rangle(M_{\text{vir}})$ is well characterised by the evolution of M_* , unlike the findings of Jing & Suto (2002) who predict a much steeper relation of $\propto M_{\text{vir}}^{-0.07}$ at high redshifts. We find that Equation (17) works well for different values of σ_8 (a variation of σ_8 results in a variation of M_* which appears as a normalisation parameter in the $\langle s \rangle(M_{\text{vir}})$ relation). Also worth noting is that at higher redshift the possible broken power-law behaviour disappears, but if it were truly due to M_* we would expect this, because already by $z = 1$ M_* is below our mass resolution.

We find that the $\langle s \rangle(M_{\text{vir}})$ at $z = 0$ for galaxy mass halos is ~ 0.6 with a dispersion of 0.1. This result is in good agreement with only one estimate for the axial ratio of the Milky Way (MW) halo. Helmi (2004) claims that a study of the M giants in the leading edge of the stream tidally stripped from the Sagittarius dwarf galaxy leads to a best fit prolate halo with $s = 0.6$. After analysis of the same data, Law et al. (2005) confirm this finding. Other studies (Ibata et al. 2001; Majewski et al. 2003; Martínez-Delgado et al. 2004) which examined different aspects of these streams concluded that the MW halo is oblate and nearly spherical with $q \gtrsim 0.8$. If the shape of the MW halo is truly this spherical, it is either at least 2σ more spherical than the median, or else baryonic cooling has had a large effect on the shape of the dark matter halo (see e.g., Kazantzidis et al. 2004).

Describing halo shapes by the triaxiality parameter T introduced by Franx et al. (1991), we find that the majority of halos are prolate with the fraction of halos being prolate increasing for halos with $M_{\text{vir}} > M_*$. Since halo shapes are closely connected to their internal velocity structure, we compute the angular momentum and the velocity anisotropy tensor and relate them to both the orientation of the halo and the triaxiality. In agreement with previous studies we find that the angular momentum is highly correlated with the smallest axis of the halo and that the principal axes of the velocity anisotropy tensor tend to be highly aligned with the principal axes of the halo. The strong alignment of all three axes of the two tensors is remarkable since the velocity tensor tends to be more spherical, thus the determination of its axes might be degenerate which would disturb the correlation with the spatial axes. If the accretion of matter determines the velocity tensor the tight correlation between velocity tensor and density shape argues for a determination of the halo shape by merging processes.

Finally we examine the evolution of shapes by following the merger trees of the individual halos. We find that the different mass accretion histories of halos cannot fully explain the observed dispersion about the mean s within fixed mass bins. It is likely that an analysis of the three dimensional accretion is essential for the explanation of the dispersion at a fixed value of mass and a_c . However, halos with earlier formation times (lower a_c) tend to be more spherical at $z = 0$. Furthermore, there is a pattern of halos becoming

spherical at a more rapid rate for halos that formed earlier and this rate appears to be independent of the final mass. The evolution of the shape for $a > a_c + 0.1$ is well described by

$$\langle s \rangle(a) \propto (a - a_c)^\nu, \quad (18)$$

where $\nu = 1.74 \times a_c^{-0.3}$. We detect a definite trend for the transformation from highly aspherical to more spherical halo shapes after a_c . The change of s seems to be less dependent on the total halo mass but strongly influenced by the relative mass increase since a_c which suggests that halos are becoming more spherical with time due to a change in the accretion pattern after a_c from a directional to a more spherical mode.

ACKNOWLEDGEMENTS

We thank Anatoly Klypin for running some of the simulations which are used in this work and for help with the others. We also thank Volker Springel and Eric Hayashi for helpful private communications. The L120_{0.9r} and L80_{0.9b} were run on the Columbia machine at NASA Ames. The L80_{0.9a}, L80_{0.75}, and L120_{0.9} were run on Seaborg at NERSC. BA and JRP were supported by a NASA grant (NAG5-12326) and a National Science Foundation (NSF) grant (AST-0205944). AVK was supported by the NSF under grants AST-0206216 and AST-0239759, by NASA through grant NAG5-13274, and by the Kavli Institute for Cosmological Physics at the University of Chicago. RHW was supported by NASA through Hubble Fellowship HF-01168.01-A awarded by Space Telescope Science Institute. JSB was supported by NSF grant AST-0507816 and by startup funds at UC Irvine. This research has made use of NASA's Astrophysics Data System Bibliographic Services.

APPENDIX A: RESOLUTION TESTS

A potential source of systematic error in the determination of halo shapes is the limited number of particles involved for low mass halos. In Figure A1 we show the result of a Monte Carlo (MC) test. Our dark matter halos are adequately described by an elliptical NFW density profile independently of cosmological model. Therefore, in the figure we show the result of applying the reduced tensor method of Equation (5) to MC halos built to have an ellipsoidal NFW profile. The axial ratios of the MC halos are drawn from Gaussian distributions of mean $\langle s \rangle = 0.7$ and $\langle q \rangle = 0.85$, and dispersion $\sigma = 0.1$. Approximately 450 halos were generated, each having ~ 1000 particles, in order to have a catalogue comparable to the sample of halos in the L80_{0.9} box with mass in the range $M_{\text{vir}} = 10^{11.3} - 10^{11.7} h^{-1} M_\odot$. The scatter plot shows that individual values of s determined at $0.3R_{\text{vir}}$ which contains roughly 300 of the 1000 particles in the halo. The recovered shape can be in error by up to ~ 0.1 . However, the scatter and mean of the distribution are very well determined by the inertia tensor method. The inset shows the histogram for the input values of the MC halos (solid line), and the histogram for the output values (i.e. determined by the tensor method; dotted line). Therefore, we conclude that the tensor method underestimates s by only 0.03 for halos

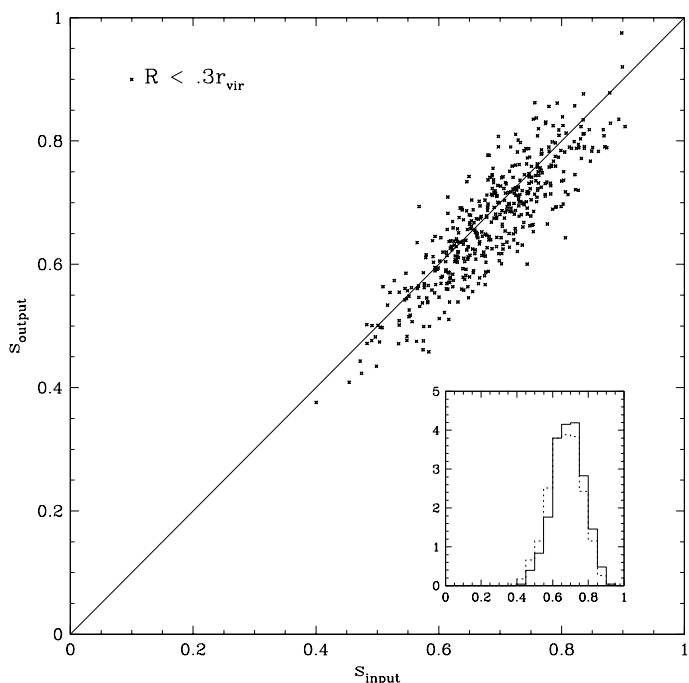


Figure A1. Results of applying our shape determination procedure at $0.3R_{\text{vir}}$ to 450 Monte Carlo halos produced with determined axial ratios. We found that the error in the recovered value of s could be as large as ~ 0.1 .

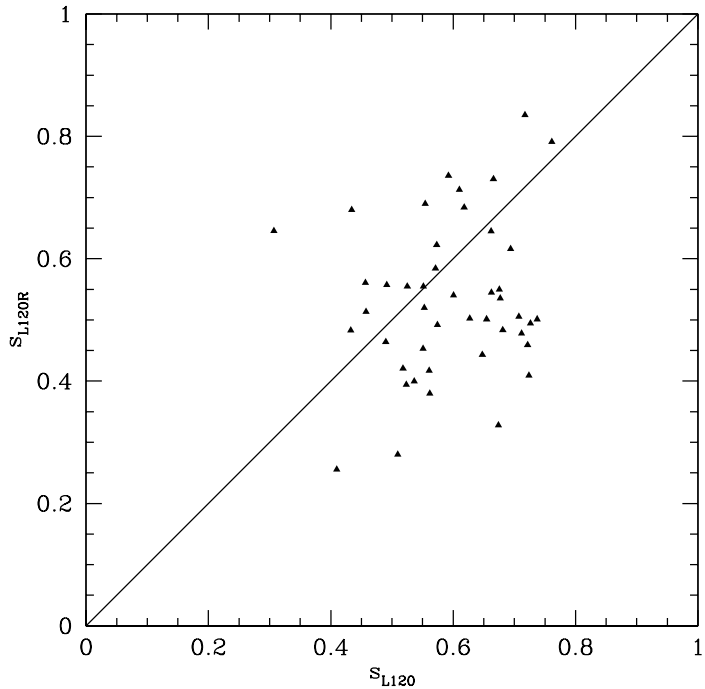


Figure A3. A direct comparison of the axial ratios of the most massive halos in the L120_{0.9r} simulation to the corresponding halos in the L120_{0.9} simulation.

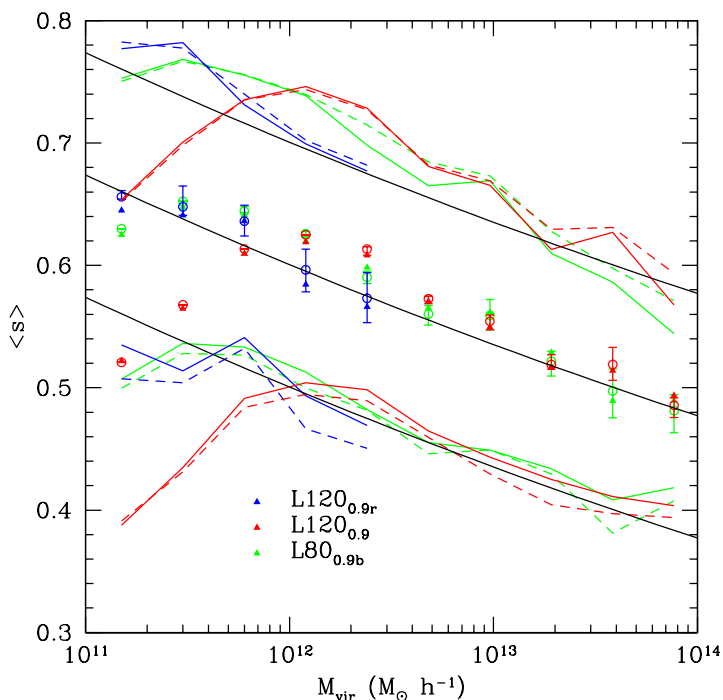


Figure A2. $\langle s \rangle$ versus mass. This plot is a replica of Figure 1 except we show mass bins below the determined resolution limit.

of this mass. For halos of mass $M_{\text{vir}} \sim 10^{11.9} h^{-1} M_{\odot}$, the error falls to 0.01.

The one problem with the above test is that we are attempting to recover shapes from smooth halos. In reality halos have substructure and the substructure must play a role in the shape of the halo. The presence of dense lumps close to the core will bias $\langle s \rangle$ to lower values relative to values determined from isodensity shells. In order to test our ability to recover the axial ratios in a cosmological simulation we determine the mean shape of halos down to very low masses for all of our simulations and then compare them to one another. The main difference between this test and the previous one is that the halos in the cosmological simulations contain substructure, but we do not know a priori what the distribution of shapes should be. In Figure A2 we have plotted the shapes of halos down to very low particle numbers. There appear to be two resolution effects at work here. The first effect is an extension of the result we found in the MC test above. At small particle number the recovered shape becomes very aspherical and all of the simulations turn over at the same number of particles. For all of the simulations the turnover is detected at ~ 3000 particles within R_{vir} (which is ~ 1000 particles within $0.3R_{\text{vir}}$, where we are determining the shape). This is consistent with our MC tests. At higher particle numbers there seems to be another effect driven by the particle number and not the mass. Halos containing $n_p < 7000$ particles for any given simulation show a trend of becoming more spherical on average than the simulations of higher resolution for the same mass. In Figure A3 we show the determined value for s for the most massive halos shared by the L120_{0.9} simulation and the resimulated subregion, L120_{0.9r}. We find that halos

shapes between the two simulations can differ by as much as 0.15 in s . This is not unexpected because in the resimulation process the identical halos are captured at slightly different times. The main point here is that the average value of s is lower in the higher resolution simulation for the same halos by ~ 0.05 .

REFERENCES

- Allgood B., 2005, PhD Thesis: Shapes and Orientations of Dark Matter Halos
- Bailin J., Kawata D., Gibson B., Steinmetz M., Navarro J., Brook C., Gill S., Ibata R., Knebe A., Lewis G., Okamoto T., 2005, *ApJL*, 627, L17
- Bailin J., Steinmetz M., 2005, *ApJ*, 627, 647
- Barnes J., Efstathiou G., 1987, *ApJ*, 319, 575
- Bryan G. L., Norman M. L., 1998, *ApJ*, 495, 80
- Bullock J. S., 2002, in Proceedings of the Yale Cosmology Workshop "The Shapes of Galaxies and Their Dark Matter Halos", New Haven, Connecticut, USA, 28-30 May 2001. Priyamvada Natarajan, Ed.. Singapore: World Scientific, 2002, [astro-ph/0106380](#) Shapes of dark matter halos. p. 109
- Buote D. A., Xu G., 1997, *MNRAS*, 284, 439
- Dubinski J., 1994, *ApJ*, 431, 617
- Dubinski J., Carlberg R. G., 1991, *ApJ*, 378, 496
- Faltenbacher A., Allgood B., Gottloeber S. amd Yepes G., Hoffman Y., 2005, *MNRAS* in press ([astro-ph/0501452](#))
- Flores R. A., Allgood B., Kravtsov A. V., Primack J. R., Buote D. A., Bullock J. S., 2005, *MNRAS* submitted [astro-ph/0508226](#)
- Franx M., Illingworth G., de Zeeuw T., 1991, *ApJ*, 383, 112
- Frenk C. S., White S. D. M., Davis M., Efstathiou G., 1988, *ApJ*, 327, 507
- Helmi A., 2004, *ApJL*, 610, L97
- Hoekstra H., Yee H. K. C., Gladders M. D., 2004, *ApJ*, 606, 67
- Hopkins P. F., Bahcall N. A., Bode P., 2005, *ApJ*, 618, 1
- Ibata R., Lewis G. F., Irwin M., Totten E., Quinn T., 2001, *ApJ*, 551, 294
- Jing Y. P., Mo H. J., Borner G., Fang L. Z., 1995, *MNRAS*, 276, 417
- Jing Y. P., Suto Y., 2002, *ApJ*, 574, 538
- Kasun S. F., Evrard A. E., 2004, *ApJ* submitted ([astro-ph/0408056](#))
- Katz N., 1991, *ApJ*, 368, 325
- Kazantzidis S., Kravtsov A. V., Zentner A. R., Allgood B., Nagai D., Moore B., 2004, *ApJL*, 611, L73
- Klypin A., Kravtsov A. V., Bullock J. S., Primack J. R., 2001, *ApJ*, 554, 903
- Klypin A. A., Gottlöber S., Kravtsov A. V., Khokhlov A. M., 1999, *ApJ*, 516, 530
- Knebe A., Gill S. P. D., Gibson B. K., Lewis G. F., Ibata R. A., Dopita M. A., 2004, *ApJ*, 603, 7
- Kolokotronis V., Basilakos S., Plionis M., Georgantopoulos I., 2001, *MNRAS*, 320, 49
- Kravtsov A. V., Berlind A. A., Wechsler R. H., Klypin A. A., Gottlöber S., Allgood B., Primack J. R., 2004, *ApJ*, 666, 0
- Kravtsov A. V., Klypin A. A., Khokhlov A. M., 1997, *ApJS*, 111, 73
- Law D. R., Johnston K. V., Majewski S. R., 2005, *ApJ*, 619, 807
- Lee J., Suto Y., 2003, *ApJ*, 585, 151
- Majewski S. R., Skrutskie M. F., Weinberg M. D., Ostriker J. C., 2003, *ApJ*, 599, 1082
- Mandelbaum R., Hirata C. M., Broderick T., Seljak U., Brinkmann J., 2005, *MNRAS* submitted ([astro-ph/0507108](#))
- Martínez-Delgado D., Gómez-Flechoso M. Á., Aparicio A., Carrera R., 2004, *ApJ*, 601, 242
- McMillan S. L., Kowalski M. P., Ulmer M. P., 1989, *ApJS*, 70, 723
- Merrifield M. R., 2004, in IAU Symposium The Galactic Halo and CDM. p. 431
- Mohr J. J., Evrard A. E., Fabricant D. G., Geller M. J., 1995, *ApJ*, 447, 8
- Navarro J. F., Frenk C. S., White S. D. M., 1996, *ApJ*, 462, 563
- Olling R. P., Merrifield M. R., 2000, *MNRAS*, 311, 361
- Springel V., White S. D. M., Hernquist L., 2004, in IAU Symposium The shapes of simulated dark matter halos. p. 421
- Tasitsiomi A., Kravtsov A. V., Gottlöber S., Klypin A. A., 2004, *ApJ*, 607, 125
- Thomas P. A., Colberg J. M., Couchman H. M. P., Efstathiou G. P., Frenk C. S., Jenkins A. R., Nelson A. H., Hutchings R. M., Peacock J. A., Pearce F. R., White S. D. M., 1998, *MNRAS*, 296, 1061
- Tormen G., 1997, *MNRAS*, 290, 411
- Vitvitska M., Klypin A. A., Kravtsov A. V., Wechsler R. H., Primack J. R., Bullock J. S., 2002, *ApJ*, 581, 799
- Warren M. S., Quinn P. J., Salmon J. K., Zurek W. H., 1992, *ApJ*, 399, 405
- Wechsler R. H., Bullock J. S., Primack J. R., Kravtsov A. V., Dekel A., 2002, *ApJ*, 568, 52
- Zentner A. R., Berlind A. A., Bullock J. S., Kravtsov A. V., Wechsler R. H., 2005, *ApJ*, 624, 505
- Zentner A. R., Kravtsov A. V., Gnedin O. Y., Klypin A. A., 2005, *ApJ*, 629, 219